Pure appl. geophys. 165 (2008) 373–407
0033–4553/08/020373–35
DOI 10.1007/s00024-008-0309-9

© Birkhäuser Verlag, Basel, 2008

Pure and Applied Geophysics

Estimation of Nonlinear Soil Behavior During the 1999 Chi-Chi, Taiwan, Earthquake

O.V. Pavlenko[1] and K.-L. Wen[2]

Abstract—The 1999 Chi-Chi, Taiwan, earthquake ($M_w = 7.6$) was one of the strongest earthquakes in recent years recorded by a large number of strong-motion devices. Though only surface records are available, the obtained strong-motion database indicates the variety of ground responses in the near-fault zones. In this study, accelerograms of the Chi-Chi earthquake were simulated at rock and soil sites, and models of soil behavior were constructed at seven soil sites (TCU065, TCU072, TCU138, CHY026, CHY104, CHY074, and CHY015), for which parameters of the soil profiles are known down to depths of at least ~70 m and at 24 other soil sites, for which parameters of the soil profiles are known down to 30–40 m; all the sites were located within ~50 km from the fault. For reconstructing stresses and strains in the soil layers, we used a method similar to that developed for the estimation of soil behavior based on vertical array records. As input for the soil layers, acceleration time histories simulated by stochastic finite-fault modelling with a prescribed slip distribution over the fault plane were taken. In spite of the largeness of the earthquake's magnitude and the proximity of the studied soil sites to the fault plane, the soil behavior at these sites was relatively simple, i.e., a fairly good agreement between the spectra of the observed and simulated accelerograms and between their waveforms was obtained even in cases where a single stress-strain relation was used to describe the behavior of whole soil thickness down to ~70–80 m during strong motion. Obviously, this is due to homogeneity in the characteristics of soil layers in depth. At all the studied sites, resonant phenomena in soil layers (down to ~40–60 m) and nonlinearity of soil response were the main factors defining soil behavior. At TCU065, TCU110, TCU115, CHY101, CHY036, and CHY039 liquefaction phenomena occurred in the upper soil layers, estimated strains achieved ~0.6–0.8%; at other stations, maximum strains in the soil layers were as high as 0.1–0.4%, according to our estimates. Thus, valuable data on the *in situ* soil behavior during the Chi-Chi earthquake was obtained. Similarity in the behavior of similar soils during the 1995 Kobe, 2000 Tottori (Japan), and Chi-Chi (Taiwan) earthquakes was found, indicating the possibility of forecasting soil behavior in future earthquakes. In the near-fault zones of the three earthquakes, "hard-type" soil behavior and resonant phenomena in the upper surface layers prevail, both leading to high acceleration amplitudes on the surface.

Key words: 1999 Chi-Chi earthquake, Nonlinear soil behavior, Liquefaction, Stress-strain relations.

1. Introduction

A destructive earthquake of magnitude $M_w = 7.6$ and depth of 7.5 km occurred in central Taiwan with its epicenter near the town of Chi-Chi on September 21, 1999. The

[1] Institute of Physics of the Earth, Russian Academy of Sciences, B. Gruzinskaya 10, Moscow 123995, Russia. E-mail: olga@ifz.ru

[2] National Center for Research in Earthquake Engineering, 200, Sec. 3, Hsin-hai Rd, Taipei 106, Taiwan, R.O.C. E-mail: wenkl@earth.ncu.edu.tw

earthquake had a predominantly thrust focal mechanism, and the surface rupture was mapped over a distance of $\sim$100 km in a SN direction. Field observations show the greatest surface offset to be more than 8 meters vertically, occurring near the northern end of the fault. The earthquake triggered more than 400 strong motion devices across Taiwan. The strong-motion wavefield was captured by a dense network of stations, and the obtained records represent one of the most complete strong-motion databases to date. The majority of near-fault records were obtained at soil sites (virtually all stations on the footwall of the fault are soil stations); these records show signs of nonlinearity in soil response, such as, predominating low-frequency components in oscillations, smoothed spectral shapes close to the form of $E(f) \sim f^{-n}$ in cases of strong nonlinearity (PAVLENKO and IRIKURA, 2005), and characteristic spiky waveforms (ARCHULETA, 1998).

The possibilities of studying soil behavior during the 1999 Chi-Chi earthquake are restricted by the fact that only surface records of the earthquake are available. A single vertical array at Dahan, located on dense soils, did record this earthquake but at a rather long distance ($\sim$80 km) from the fault plane (CHIU, 2001; PAVLENKO and LOH, 2003). Nonlinearity of soil response during the Chi-Chi earthquake has been previously studied by ROUMELIOTI and BERESNEV (2003) and by K.-L. Wen (Wen, pers. communic.). Since only surface records of the Chi-Chi earthquake are available, in these studies, spectra of acceleration time histories at soil sites are investigated in order to find characteristics of soil nonlinearity. Lower amplification of seismic waves in some frequency bands during strong ground motions compared to weaker ones (aftershocks) is interpreted as an indicator of nonlinearity in soil response, and respective quantitative characteristics are introduced.

In ROUMELIOTI and BERESNEV (2003), nonlinearity of soil response during the Chi-Chi earthquake is studied by comparing amplification of seismic waves at soil sites during the main shock and aftershocks of the Chi-Chi earthquake. The authors simulate records of the Chi-Chi earthquake by the stochastic finite-fault method and calibrate these against the data recorded at twenty-four rock sites. Then soil-site records are simulated using the linear-response assumption whereby the simulated soil-site input motions are amplified by weak-motion amplification functions, estimated by the spectral ratio technique from the aftershock records. Their comparison with actual observations allows the authors to reveal an average reduction in strong-motion amplification to about 0.5–0.6 of that in weak motions, with an acceleration "threshold" for detectable nonlinearity near 200–300 cm/s^2. The conclusions of this study confirm in the whole earlier obtained average estimates of decreasing amplification of seismic waves during strong ground motion at soil sites; however, the authors emphasize a large interstation response variability, which did not allow them to derive a statistically significant difference in weak and strong-motion amplifications based on the responses available at the studied sixteen stations.

The present study is aimed at a more detailed investigation of soil response during the 1999 Chi-Chi earthquake. Accounting for the observed variability of soil response patterns, we concentrate on constructing models of soil behavior at separate stations, instead of studying average regularities, which seems to be more informative in this case.

To do this, we simulate acceleration time histories at soil sites at the bottoms of soil layers and then calculate their propagation up to the surface, selecting models of soil behavior that show best fit to the observed acceleration records at the surface. Models of soil behavior during the Chi-Chi earthquake are constructed for seven soil sites, for which parameters of the soil profiles were known down to depths of at least 70 m, and for twenty-four soil stations, for which the profiling data were available down to depths of $\sim$30–40 m. Thus, models of soil behavior during the Chi-Chi earthquake are constructed for thirty-one soil sites located within $\sim$50 km of the fault plane. In constructing models of soil behavior during the Chi-Chi earthquake, we use our previous experience in studying the soil behavior during the 1995 Kobe and 2000 Tottori (Japan) earthquakes based on vertical array records (PAVLENKO and IRIKURA, 2003, 2005, 2006). The constructed models of soil behavior testify to the strong nonlinearity of the soil response in the near-fault zones of the Chi-Chi earthquake.

2. *Simulation of Acceleration Time Histories of the Chi-Chi Earthquake at Rock Sites*

The epicenter of the 1999 Chi-Chi earthquake, the surface rupture and locations of eighteen rock and thirty one soil stations studied in this work are shown in Figure 1. We used strong-motion data of the Chi-Chi earthquake disseminated on CD-ROM by LEE *et al*. (2001b), accelerograms provided by the website of the Central Weather Bureau (CWB) of Taiwan and profiling data provided by the National Center for Research in Earthquake Engineering (NCREE) of Taiwan.

Firstly, we calculated accelerograms of the Chi-Chi earthquake at rock sites. Since the purpose of our study is to simulate soil behavior, we tried to simulate most accurately motion at the "input" of the soil layers. In the calculations, we used Boore's stochastic approach (BOORE, 2003); however, we modified his method to account for the dimensions of the source and slip distribution over the fault plane.

The availability of such a complete near-source strong-motion dataset being generated by the Chi-Chi earthquake, combined with broadband teleseismic displacement waveforms, well-distributed Global Positioning System (GPS) data, and the considerable volume of geological and geophysical data collected in Taiwan over the past decades has provided an excellent opportunity to study the kinematic source process of this large earthquake, and various versions of slip distribution over the fault plane have been obtained (MA *et al*., 2001; ZENG and CHEN, 2001; OGLESBY and DAY, 2001; WU *et al*., 2001; CHI *et al*., 2001; WANG *et al*., 2001). In our calculations we used the slip distribution obtained by W.-C. Chi, D. Dreger and A. Kaverina (CHI *et al*., 2001). Velocity waveforms recorded at 21 stations were inverted for spatial variation in slip on a planar fault model composed of 416 subfaults, each with a dimension of 3.5 km by 3.5 km. To account for possible temporal source complexity, each subfault was allowed to slip within 10 overlapping 3-second time windows. The kinematic rupture process was studied in detail in this work (CHI *et al*., 2001), and various inversion problems were

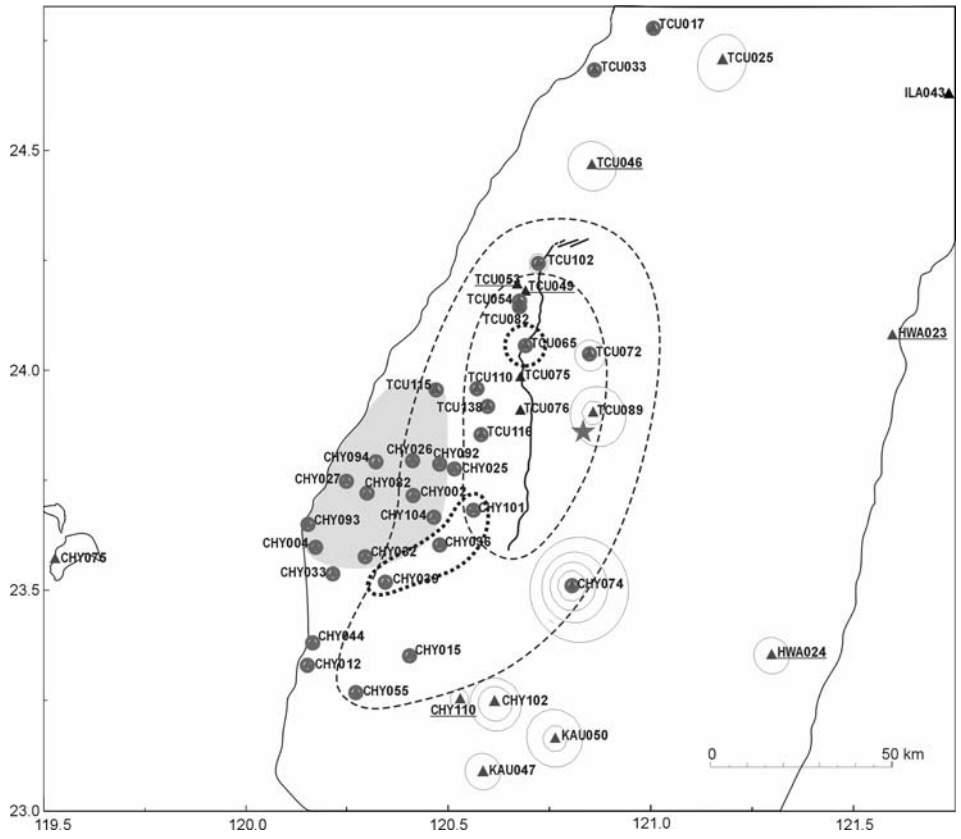

Figure 1

Map showing the epicenter of the 1999 Chi-Chi earthquake (star), the surface rupture and locations of eighteen rock (black triangles) and thirty one soil stations (gray triangles in circles) used in this work. Dashed lines bound the areas where $R_c < 15$ km and $R_c < 50$ km. Dotted lines mark liquefaction areas, and the area, where basin-induced surface waves were identified, is marked by grey color.

discussed and justified, with error analysis being performed; the results of the inversion are provided on CD-ROM (Lee *et al.*, 2001b) and could be easily inserted in the calculations.

In simulating accelerograms of the Chi-Chi earthquake, we represented its source (119 km by 35 km) as a set of subfaults with dimensions, locations, parameters of radiation, as well as the method for summarizing their energy being selected in accordance with recommendations by Gusev and Pavlov (2006), who studied all aspects of earthquake ground motion simulation for many years and achieved success in this area (Bazzurro *et al.*, 2001) (we represented the space-time structure of the slip rate function through a grid of subsources, where the cell size of a subsources was defined by site-to fault distance; onset times and seismic moments of subsources were determined by the

generalized Haskell source model; time histories of subsources were taken uncorrelated; final slip and rupture velocity were defined as random functions and varied along x and y; each point subsource was randomly shifted from a node of the perfect regular grid (typically by 0.3–0.6 cell size)). Each of the subfaults was assigned an ω^2 spectrum. Some other parameters used in the calculations, such as, spatial orientation of the fault plane, the nucleation point, coordinates and depth of the hypocenter, slip velocity and slip distribution over the fault plane, were derived from the paper by CHI *et al*. (2001). We selected the subfault dimension of 7 km by 7 km, averaging slips over the adjacent areas of 3.5 km by 3.5 km of the "preferred model" by CHI *et al*. (2001); the estimated temporal variations of the rupture process were also averaged, and the final simplified and smoothed representation of the rupture process was obtained (Fig. 2). This representation was used for generating two spatial weight functions, "dip-slip" and "left-lateral strike-slip", indicating the relative contributions of the subfaults in the two directions. Time delays for subfault radiation were calculated based on rupture velocity, which was taken as constant and equal to 2.6 km/s according to (CHI *et al*., 2001). Subfault radiation was simulated as stochastic, empirically attenuated to the observation site, and summarized with introducing slight random variations in subfault locations and rupture velocity. Local rise times were taken as equal for all subfaults. Thus, acceleration time histories in "dip-slip" and "left-lateral strike-slip" directions were calculated with spatial weight functions (Fig. 2) applied to subfault radiation and rotated in NS and EW

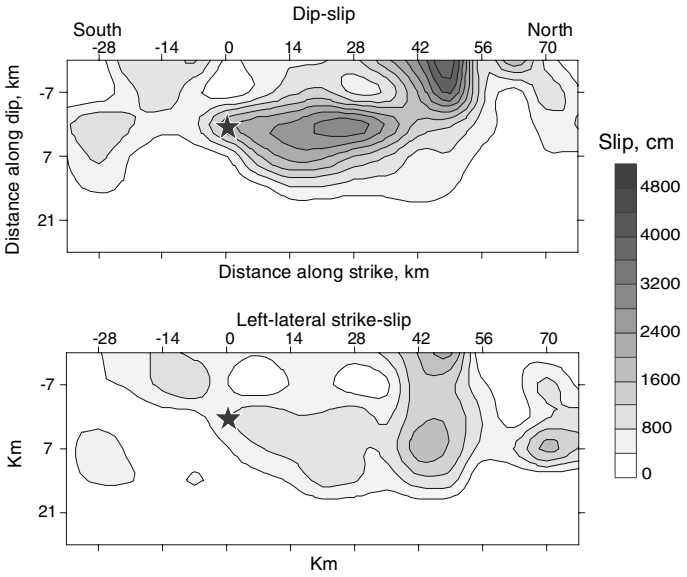

Figure 2
Distribution of slip over the fault plane of the Chi-Chi earthquake used in our simulations: Averaged slip distribution of the "preferred model" by CHI *et al*. (2001). Star indicates the hypocenter.

Table 1

Locations of rock stations used in simulations

Station code	Latitude (°)	Longitude (°)	Elevation (m)	R_c (km)	Distance to the closest subfault (km)	Weighted aver. dist. to subfaults (km)
North (forward direction):						
TCU049	24.179	120.690	129	10	6.5	28.3
TCU053	24.194	120.669	133	15	5.4	28.9
TCU046	24.468	120.854	231	50	13.3	44.4
TCU025	24.707	121.176	310	50	36.8	80.3
ILA043	24.629	121.735	36	50	88.6	118.9
ILA052	24.609	121.849	20	50	99.9	128.3
East and West (normal to the fault):						
TCU075	23.983	120.678	104	15	6.8	31.3
TCU076	23.908	120.676	99	10	7.5	34.8
TCU089	23.904	120.857	705	12	16.2	38.1
HWA023	24.080	121.596	30	50	79.2	93.5
HWA024	23.352	121.297	260	50	57.7	103.2
CHY075	23.567	119.555	11	50	100.9	135.9
South (backward direction):						
CHY102	23.246	120.614	560	50	33.2	95.0
CHY110	23.252	120.530	215	50	32.7	95.8
KAU050	23.163	120.757	640	50	41.9	103.2
KAU047	23.082	120.583	278	50	50.6	112.6
TTN024	22.973	121.108	277	50	70.1	129.7
KAU077	22.747	120.723	835	50	85.6	147.2

directions. Simulated acceleration time histories at rock sites were compared to the observed ones, and calibration of the simulation procedure was performed, i.e., parameters characterizing source and path effects were found, which show the best fit to the observations.

We calculated acceleration time histories at all near-fault rock sites, for which good-quality acceleration records of the Chi-Chi earthquake at two horizontal components are available. We found 18 such sites; their coordinates, elevations, characteristic distances R_c (discussed below), the distances to the closest subfaults, and weighted (weights being proportional to the subfault radiation intensity) average distances to subfaults are given in Table 1. Some stations classified in (LEE *et al.*, 2001a) as Class B Sites, have shown amplification at low frequencies (the problem is discussed in (LEE *et al.*, 2001a)), which we interpreted as site effects. We decided to exclude such stations (CHY042, CHY052, CHY074, CHY086, CHY109, KAU069, KAU078, ILA063, HWA022, HWA026, HWA046, HWA056, TTN018, TTN026, TTN041, TAP034, and TAP035) from the list of "rock sites" in this study. At the same time, other stations were added to this list based on the results of simulations, such as, TCU049, TCH053, TCU075 and TCU076 stations.

Figure 3 shows the results of simulations at rock sites. The observed and simulated (one of the series) accelerograms at two horizontal components and spectra of the observed and simulated (averaged over the series of simulated accelerograms)

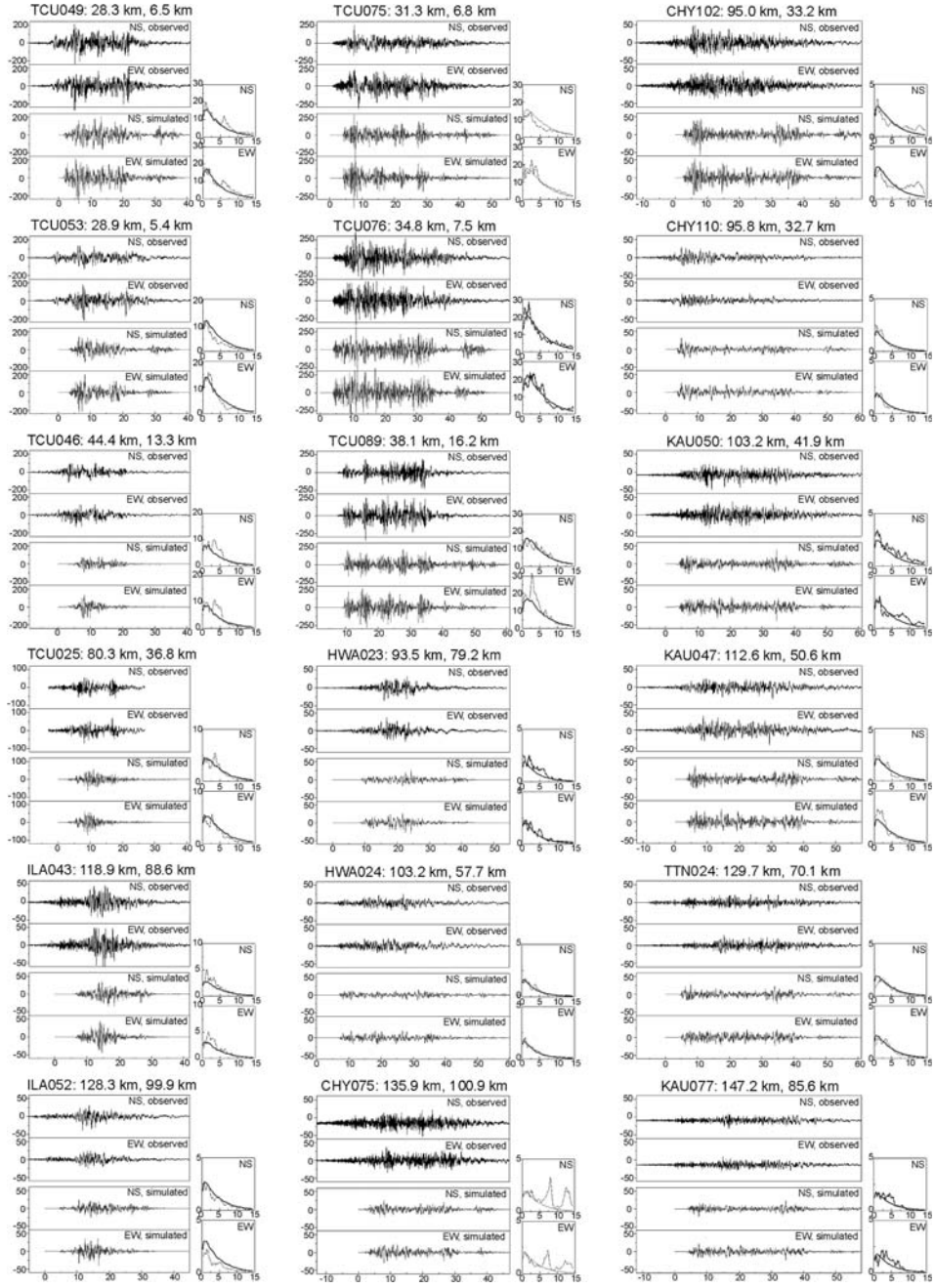

Figure 3

The results of simulations of the acceleration time histories of the Chi-Chi earthquake at rock sites: Observed and simulated accelerograms and their spectra. After the station codes weighted average distances to the subfaults and distances to the closest subfaults are shown.

accelerograms are shown. Comparison of the observed and simulated accelerograms and their spectra gives a representation of the accuracy of simulations. As seen from the figure, a rather good agreement was achieved between the observed and simulated accelerograms, and some misfit in their spectra (noticeable at stations TCU089, TCU046, CHY102, and at island station CHY075) is obviously due to local effects of wave amplification in some frequency bands.

To trace effects of directivity (GUSEV and PAVLOV, 2006), the stations are arranged according to their orientation with respect to the direction of the crack propagation (CHI *et al*., 2001). Directivity effects are clearly seen as decreased durations of acceleration time histories in forward (northern) directions and increased durations in backward (southern) directions; eastern and western directions represent intermediate cases (Fig. 3).

Table 2 shows parameters used in the simulations. The spatial orientation and dimensions of the fault plane, the coordinates and depth of the hypocenter, the slip velocity and slip distribution over the fault plane were derived from the paper by CHI *et al*. (2001). Frequency-dependent attenuation effects of the propagation path are modeled through the function $Q(f)$ as described in BOORE (2003). We assumed the relationship estimated for the Taiwan area from coda-waves by CHEN *et al*. (1989): $Q(f) = 117f^{0.77}$. Kappa operator was used for additional attenuation of the spectra (ANDERSON and HOUGH, 1984; BOORE, 2003); we took $\kappa = 0.07$ sec. Thus, these parameters were taken as the same as those used in the work by ROUMELIOTI and BERESNEV (2003), because our calculations show that these values well fit the observed data and only slightly define the simulations (i.e., their variations within some limits do not greatly influence the obtained accelerograms).

At the same time our results show that for near-fault stations, geometrical spreading is one of the most important factors defining the shapes of the acceleration time histories.

Table 2

Parameters used in simulations

Fault orientation (strike/dip)	5°/30°
Fault dimensions along strike and dip (km)	119 by 35
Coordinates of the hypocenter (lat., lon.)	23.8689, 120.84
Depth of the hypocenter (km)	8.75
Subfault dimensions (km)	7 × 7
Stress drop $\Delta\sigma$ (bars)	50
Number of subsources summed	85
$Q(f)$	$117 \cdot f^{0.77}$
Geometrical spreading	$1/r$ for $r < R_c$ km $1/R_c$ for $R_c \leq r < 150$ km
Kappa κ, (sec)	0.07
Crustal amplification	BOORE and JOYNER (1997) western North America generic rock site; at underlined stations – hard rock (BOORE, 2003)
Crustal shear-wave velocity (km/s)	3.2
Rupture velocity (km/sec)	2.6
Crustal density (g/cm^3)	2.6

For example, simulating acceleration time histories at TCU075, TCU076, TCU089, TCU072 and other near-fault stations located within the area marked by a dashed line in Figure 1 with conventional geometrical spreading relationships:

$$1/r \text{ for } r<50 \text{ km}, \quad 1/50 \text{ for } 50 \le r<150 \text{ km} \tag{1}$$

(BOORE, 2003), we obtain too strong attenuation in the medium and final parts of the simulated accelerograms; this does not satisfy the observations. As seen from Figure 3, accelerograms at these stations represent successive arrivals of groups of seismic waves of approximately equal intensity, which evidently correspond to radiation from different parts of the fault plane (subfaults). Application of conventional relationships (1) produces accelerograms with the intensity of these waves quickly decreasing with time. However, a good agreement between observations and simulations can be obtained if describing geometrical spreading by the relationship:

$$1/r \text{ for } r<R_c \text{ km}, \quad 1/R_c \text{ for } R_c \le r<150 \text{ km}, \tag{2}$$

where distance R_c varies from 10 km in the vicinity of the fault plane to 50 km beyond the area marked by the dash line in Figure 1 (Table 1). For all the stations, R_c values were found in calculations as showing the best fit to the observations. It is seen from Table 1 that $R_c < 50$ km in cases where the average removal of the station from the subfaults is less than 44–50 km. As shown below (listed in Table 3), $R_c < 50$ km also for stations located to the south of the fault plane at average distances of 50–85 km; the area of decreased R_c values is stretched in the southern direction (Fig. 1). Apparently, this effect should be attributed to peculiarities in the geometry of the earthquake source to the effects of "subsurface waveguide".

At the majority of the studied rock sites, the upper-crustal amplification was described by parameters established by BOORE and JOYNER (1997) for the western North America generic rock site. However, at some stations (underlined in Fig. 1 and Table 1) these parameters gave excessively higher amplification not corresponding to the observations, so they were changed to "hard rock" amplification parameters (BOORE, 2003), which better satisfy the observations. In simulating acceleration time histories at soil sites, we did not account for the upper-crustal amplification.

In the whole, a fairly good agreement was achieved between the observed and simulated acceleration time histories at the studied rock stations, especially in near-fault zones, in many respects because of the use of slip distribution along the fault plane (CHI *et al.*, 2001). Some disagreements between observations and simulations seem to be related to site effects and therefore are not significant within the framework of this study.

3. Simulation of Acceleration Time Histories of the Chi-Chi Earthquake at Soil Sites

At the second step of our study, we simulated acceleration time histories at soil sites and constructed models of soil behavior during the Chi-Chi earthquake, i.e., estimated

Table 3

Information on soil stations used in simulation

Station Code	Latitude (°)	Longitude (°)	Elevation (m)	R_c (km)	Closest dist. to sub-fault (km)	Aver. dist. to sub-faults (km)	Aver. V_s in upper 30 m (m/s)	Site Class (Lee *et al.*, 2001), soil composition
North:								
TCU082	24.148	120.676	84	15	5.7	28.3	476	D gravel
TCU054	24.161	120.675	99	20	6.1	28.4	454	D silt, gravel
TCU102	24.249	120.721	227	22	7.8	29.6	735	D gravel, siltstone
TCU033	24.686	120.862	6	50	16.9	64.2	450	D gravel, siltstone
TCU017	24.781	121.007	86	50	29.7	78.1	600	? gravel, mudstone
Centre:								
TCU065	**23.059**	**120.691**	**56**	**12**	**6.9**	**28.9**	**300**	**D** sandy clays, silt, gravel
TCU072	**24.041**	**120.849**	**292**	**12**	**14.9**	**32.4**	**563**	**D** colluvium, breccia, shale, siltstone
TCU110	23.962	120.570	23	14	2.4	35.5	207	E sand, clay, silt
TCU138	**23.922**	**120.596**	**37**	**12**	**3.8**	**36.2**	**605**	**D** gravel
TCU116	23.857	120.580	42	15	3.4	40.3	483	E silt, gravel
TCU115	23.960	120.469	15	35	11.4	41.6	190	E silt
South:								
CHY025	23.780	120.514	42	16	5.9	48.2	277	E silt, gravel
CHY092	23.791	120.478	34	25	9.5	49.5	260	E silt
CHY101	23.686	120.562	75	10	1.9	53.0	260	D silt, sand, gravel
CHY026	**23.799**	**120.411**	**25**	**30**	**16.1**	**53.1**	**226**	**E** sand, clay, silt
CHY002	23.719	120.413	26	25	15.0	58.1	225	E silt
CHY104	**23.670**	**120.465**	**33**	**30**	**9.5**	**58.7**	**225**	**E** sand,clay,silt
CHY094	23.794	120.321	10	50	24.9	59.7	227	E silt
CHY036	23.607	120.479	45	20	7.5	63.1	282	D silt, clay, sand, gravel
CHY082	23.724	120.298	13	50	26.6	65.4	210	E silt
CHY027	23.752	120.247	8	50	32.1	67.6	220	E silt
CHY074	**23.510**	**120.805**	**2413**	**16**	**12.8**	**67.8**	**546**	**C** sand, clay, silt-stone, breccia
CHY032	23.580	120.294	9	50	25.6	75.6	202	E silt, clay, sand
CHY039	23.521	120.344	16	30	20.8	77.3	198	E silt, clay, sand
CHY093	23.654	120.147	4	50	41.2	81.0	199	E silt, sand
CHY004	23.601	120.172	6	35	38.2	82.5	279	E silt, sand
CHY033	23.541	120.215	3	50	33.6	83.7	194	E silt, sand
CHY015	**23.355**	**120.405**	**34**	**18**	**25.9**	**89.4**	**234**	**D** silt, clay, sand
CHY044	23.383	120.164	2	50	43.0	99.4	193	E silt, sand
CHY055	23.270	120.271	8	35	41.5	103.4	240	E silt, clay, sand
CHY012	23.333	120.152	1	50	46.6	104.2	202	E silt, clay, sand

stresses and strains induced in the soil layers during strong motion. The soil behavior was studied at sites, for which the profiling data were available. At seven soil stations, such as, TCU065, TCU072, TCU138, CHY026, CHY104, CHY074, and CHY015, soil

composition, *P*- and *S*-wave velocities and the results of *SPT-N* testing are available down to depths of $\sim$70–140 m, and at other twenty four soil stations, these data are known down to $\sim$30–40 m. The coordinates of these thirty one soil stations, their elevations, distances R_c, distances to the closest subfaults, weighted average distances to the subfaults, Site Class and soil composition are given in Table 3 (seven stations, for which profiling data were available down to $\sim$70–80 m, are marked in bold). Site Classification of Taiwan free-field strong motion stations is described in LEE *et al*. (2001). Based on the available geologic and geomorphologic data, free-field strong motion station sites were classified using a scheme compatible with the 1997 Uniform Building Code (UBC) provisions. The response spectral shapes (RSS) and the horizontal-to-vertical spectral ratio (HVSR) methods and field inspections were used for checking purposes. However, some problematic sites do exist (LEE *et al*., 2001).

Concentric lines in Figure 1 mark stations with elevations above sea-level of higher than 200 m. Though topographic effects were not accounted for in simulating acceleration time histories, they could contribute to amplification or de-amplification of oscillations on the surface. The influence of topographic effects on strong motion stations in Taiwan is discussed in LEE *et al*. (2001), where a number of stations obviously influenced by surface topography are listed; none of these stations is studied in this research. Also, as seen from Figure 1 and Table 3, all the studied soil stations, except TCU072, TCU102, and CHY074, are placed in valleys, and therefore, surface topography does not influence the records. However, the influence of subsurface topography is seen in the records at some stations and discussed below.

In reconstructing stresses and strains at these stations, our previous experience in studying soil behavior during the 1995 Kobe and the 2000 Tottori earthquakes based on vertical array records was used (PAVLENKO and IRIKURA, 2003, 2004, 2005, 2006). The method for the estimation of nonlinear stress-strain relations in soil layers based on vertical array records is described in detail in PAVLENKO and IRIKURA (2003).

In this study, to estimate stresses and strains in soil layers during strong motion, we calculated the propagation of vertically incident "input" seismic waves (simulated accelerograms) up to the surface. In the calculations, we used the algorithm of nonlinear analysis by JOYNER and CHEN (1975), modified by Pavlenko so that, instead of the normalized stress-strain relations used by Joyner and Chen (similar to those obtained in laboratory experiments and described by HARDIN and DRNEVICH (1972)), any other stress-strain relations of the "hard" (declining to the stress axis at large strains) or "soft" (declining to the strain axis at large strains) types can be used to describe the soil behavior. The relations can differ for different soil layers and at different time intervals.

In our calculations, these stress-strain relations were prescribed parametrically, and differed from each other by their shape. For calculations, we have to divide the studied soil profiles into groups of layers, according to the soil composition, depth and saturation with water, and assume certain "hard" or "soft" types of stress-strain relations to different groups of layers. The choice of "hard" or "soft" types of soil behavior is based on the established regularities of the behavior of cohesive and non-cohesive soils *in situ*

in conditions of dynamic loading. It is discussed in detail in PAVLENKO and IRIKURA (2003, 2004, 2006). "Hard-type" stress-strain curves describe well the behavior of water-saturated sandy soils. Analysis of accelerograms of the 1995 Kobe and 2000 Tottori earthquakes has shown that "hard-type" soil behavior in strong ground motion is widespread and typical for sandy soils in cases when the level of underground water is above $\sim$10 m (PAVLENKO and IRIKURA, 2003, 2004, 2006). Whereas soft soils, like dry loess loams and sands, possess stress-strain relations declining to the strain axis at large strains, which are often called "soft" diagrams.

In LEE *et al*. (2001a), site classification of free-field strong-motion stations in Taiwan was performed. Based on available geologic and geomorphologic data, RSS (response spectral shapes) and the HVSR (horizontal-to-vertical spectral ratio) methods and field checks, the stations were classified using a scheme compatible with the 1997 Uniform Building Code (UBC) provisions. Ten stations, including TCU082, TCU054, NCU102, TCU065, TCU072, TCU138, CHY015, and others, were categorized as class D sites, station CHY074 as a class C site, and the rest twenty stations, such as, TCU110, TCU116, TCU115, CHY025, CHY026, CHY104, etc., as class E sites. Data on the composition and thickness of the soil layers, *P*- and *S*-wave velocities, and *SPT-N* values are taken from the National Center for Research in Earthquake Engineering (NCREE) of Taiwan.

First we have studied soil behavior at seven stations possessing the most complete information on the profiling data, such as, TCU065, TCU072, TCU138, CHY026, CHY104, CHY074, and CHY015 stations. At TCU065, CHY026, CHY104, and CHY015 stations, soil profiles in the upper $\sim$50 m, $\sim$100 m, $\sim$90 m, and $\sim$60 m, respectively, represent alternating layers of sandy clays with silt and silty soils with *S*-wave velocities increasing with depth from $\sim$160–200 m/s at the surface to 420–600 m/s at depth (parameters of the soil profiles are shown below in Figs. 4a-g). These layers are underlayed by denser colluvium soils. At TCU072, TCU138, and CHY074 stations colluvium deposits are closer to the surface. At TCU072 and CHY074 stations, *S*-wave velocities increase with depth from 250 m/s and 360 m/s, respectively, in the upper 8–10 m to $\sim$1120 m/s at depths of $\sim$70 m. At TCU138 station, the soil layers down to depths of $\sim$150 m represent mostly dense soils with *S*-wave velocities varying within $\sim$400–800 m/s.

According to *P*-wave velocities, the underground water level is rather close to the surface at all the studied sites, and therefore, "hard-type" stress-strain relations were selected to describe the behavior of upper soil layers at all the sites. In this work, to describe the behavior of the soil layers down to $\sim$70–80 m at each station, we used one "hard-type" normalized stress-strain relation. That is, we treated all the soil thickness at all the stations, except TCU065, as one group of layers. With these simple models of soil behavior, we could obtain a good agreement between observations and simulations.

At TCU065 to fit the observations, we had to apply a more complicated model: We used one "hard-type" stress-strain relation to describe the behavior of the upper $\sim$37 m

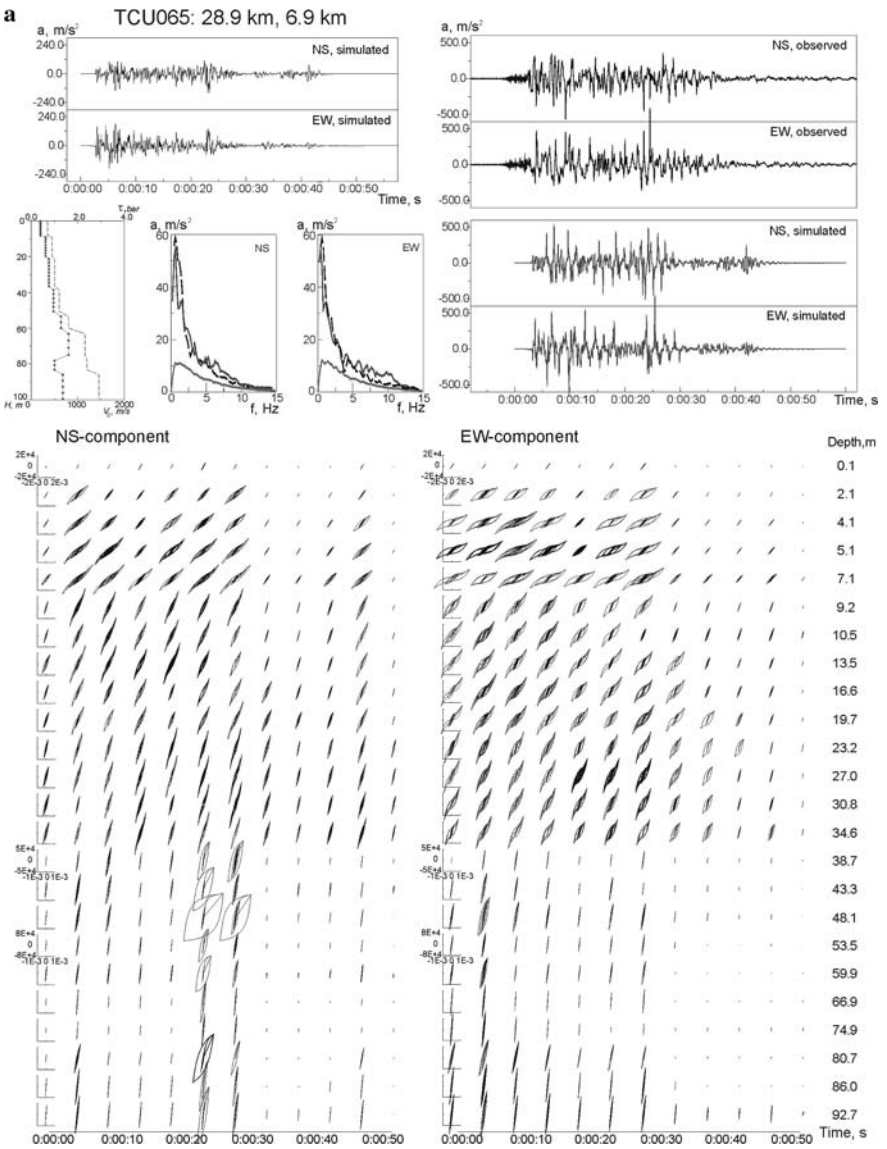

Figure 4

The results of simulations of the acceleration time histories of the Chi-Chi earthquake at soil sites: simulated accelerograms at the bottoms of the soil layers (upper left corner); below — the profiling data (V_S – solid line and τ_{max} – dashed line) and spectra of the simulated accelerograms at the bottoms of the soil layers (low-level grey line) and of the observed (dashed line) and simulated (solid line) surface accelerograms; the observed and simulated accelerograms on the surface (upper right corner), and the corresponding vertical distributions of stresses and strains in the soil layers, changing in time during the strong motion for NS and EW components: a –TCU065; b –TCU072; c –TCU138; d –CHY026; e –CHY104, f –CHY074; and g –CHY015. After the station codes weighted average distances to the subfaults and distances to the closest subfaults are shown.

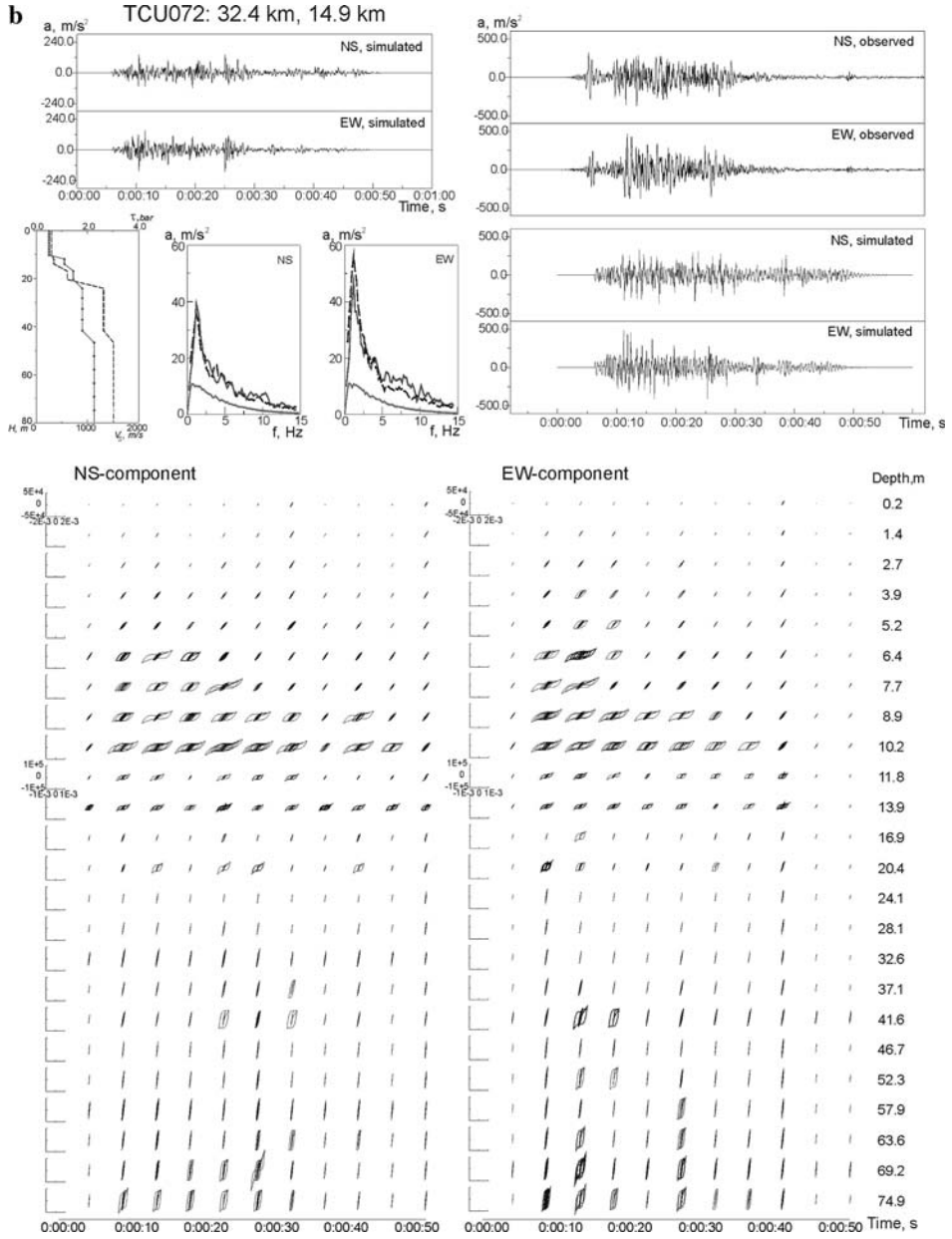

Figure 4
(Contd.)

and the stress-strain relation similar to that obtained in laboratory experiments by HARDIN and DRNEVICH (1972) to describe the behavior of the underlying more dense soil layers. It was shown in PAVLENKO and IRIKURA (2003, 2004, 2006) that these relations well

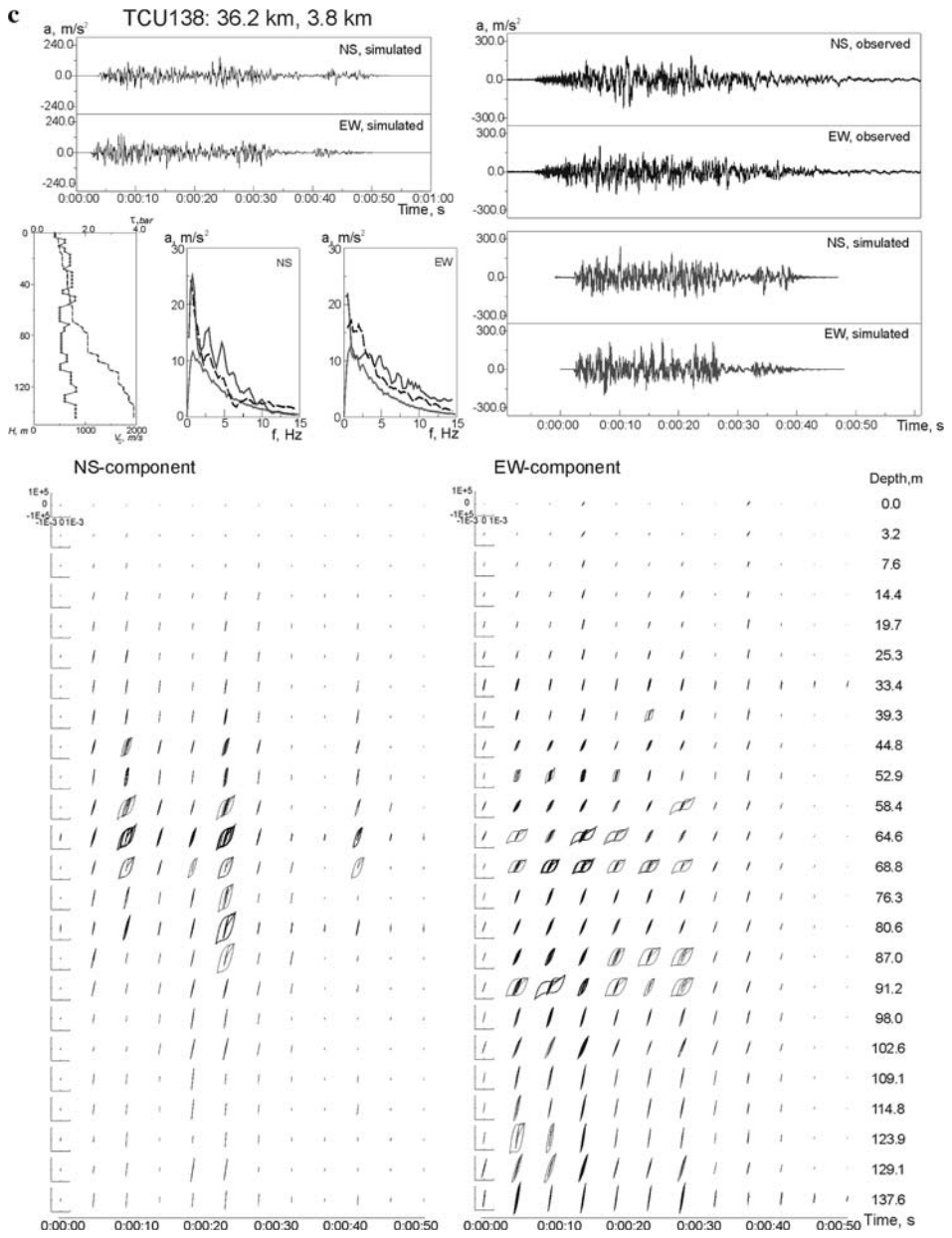

Figure 4
(Contd.)

describe the behavior of dense cohesive and non-cohesive soils *in situ* at depth. The stress and strain were normalized in the manner used by HARDIN and DRNEVICH (1972): Stress was normalized by multiplying by $1/\tau_{max}$ (where τ_{max} is shear stress in failure) and strain

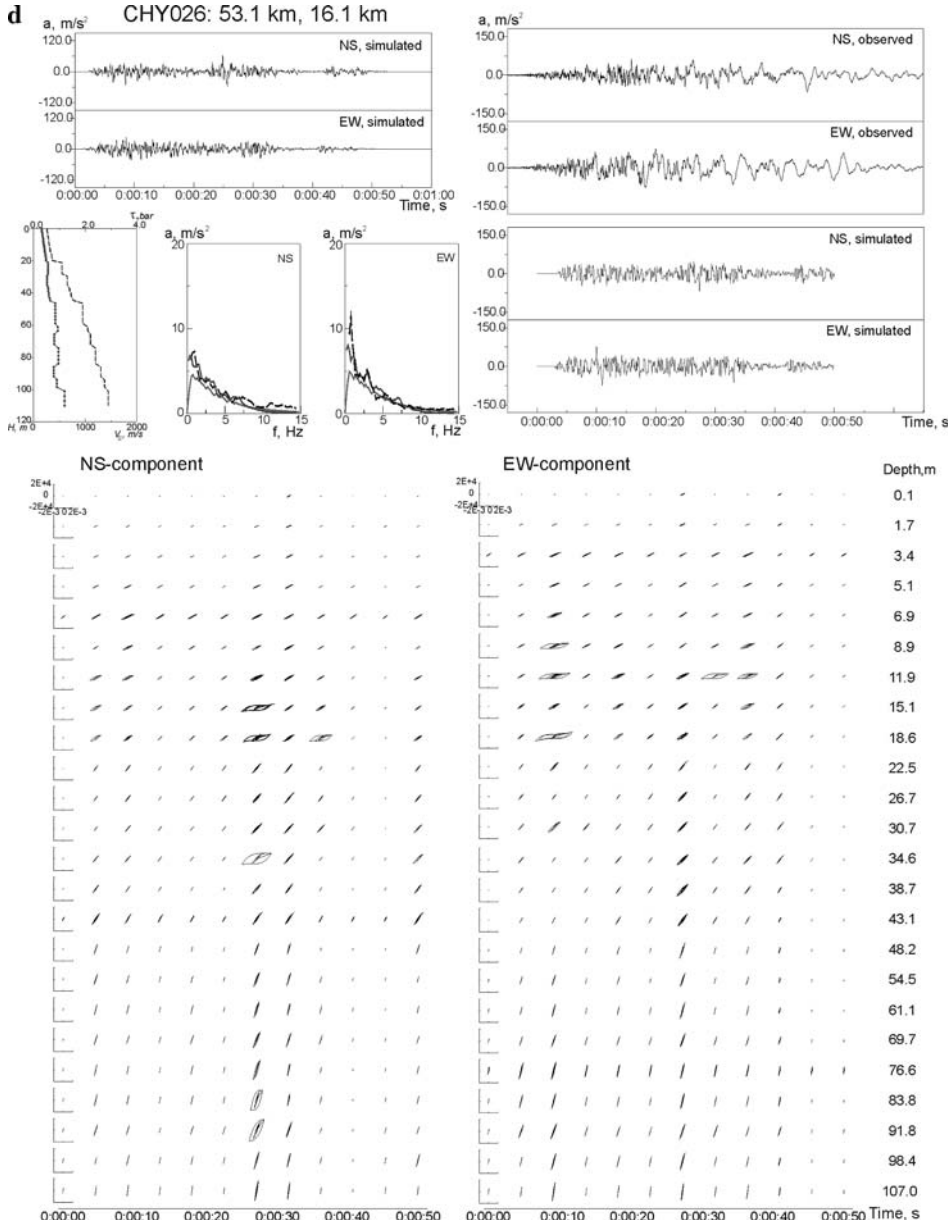

Figure 4
(Contd.)

was normalized by multiplying by G_{max}/τ_{max} (where G_{max}/τ_{max} is the low-strain modulus) (JOYNER and CHEN, 1975). The differences in the behavior of different soil layers result from differences in the values of τ_{max} and G_{max} assigned to the different layers.

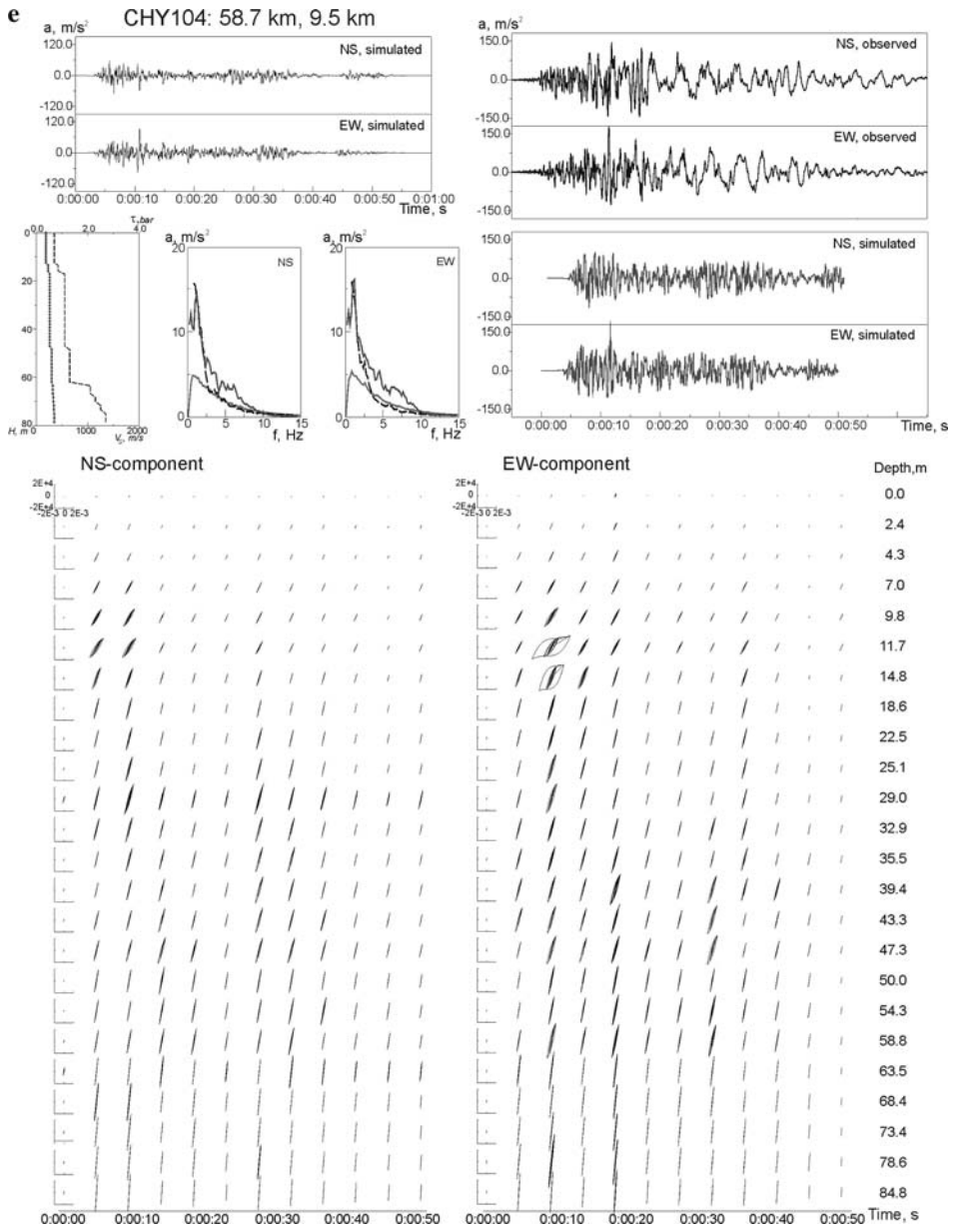

Figure 4
(Contd.)

Two hundred fifty different curves of the selected type were generated, and item-by-item examination was applied to identify the curves, showing the best-fit approximations to the observed accelerograms on the surface. “Inputs” to soil layers, i.e.,

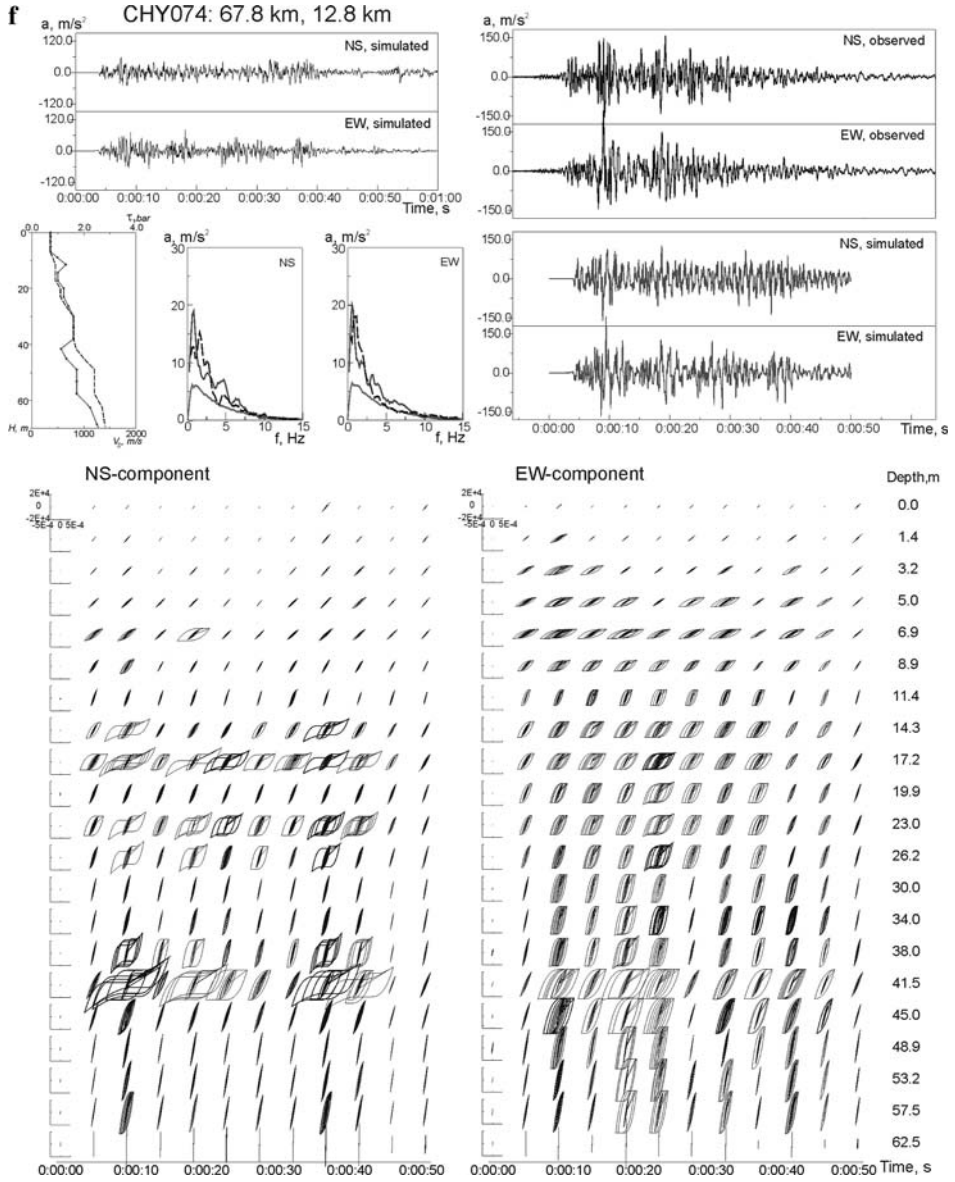

Figure 4
(Contd.)

simulated accelerograms, were used as prescribed motion at the base of the soil columns (the free surface factor was taken equal to 2, when calculating acceleration time histories at rock sites, and equal to 1 in this case). That is, we assume infinite rigidity in the

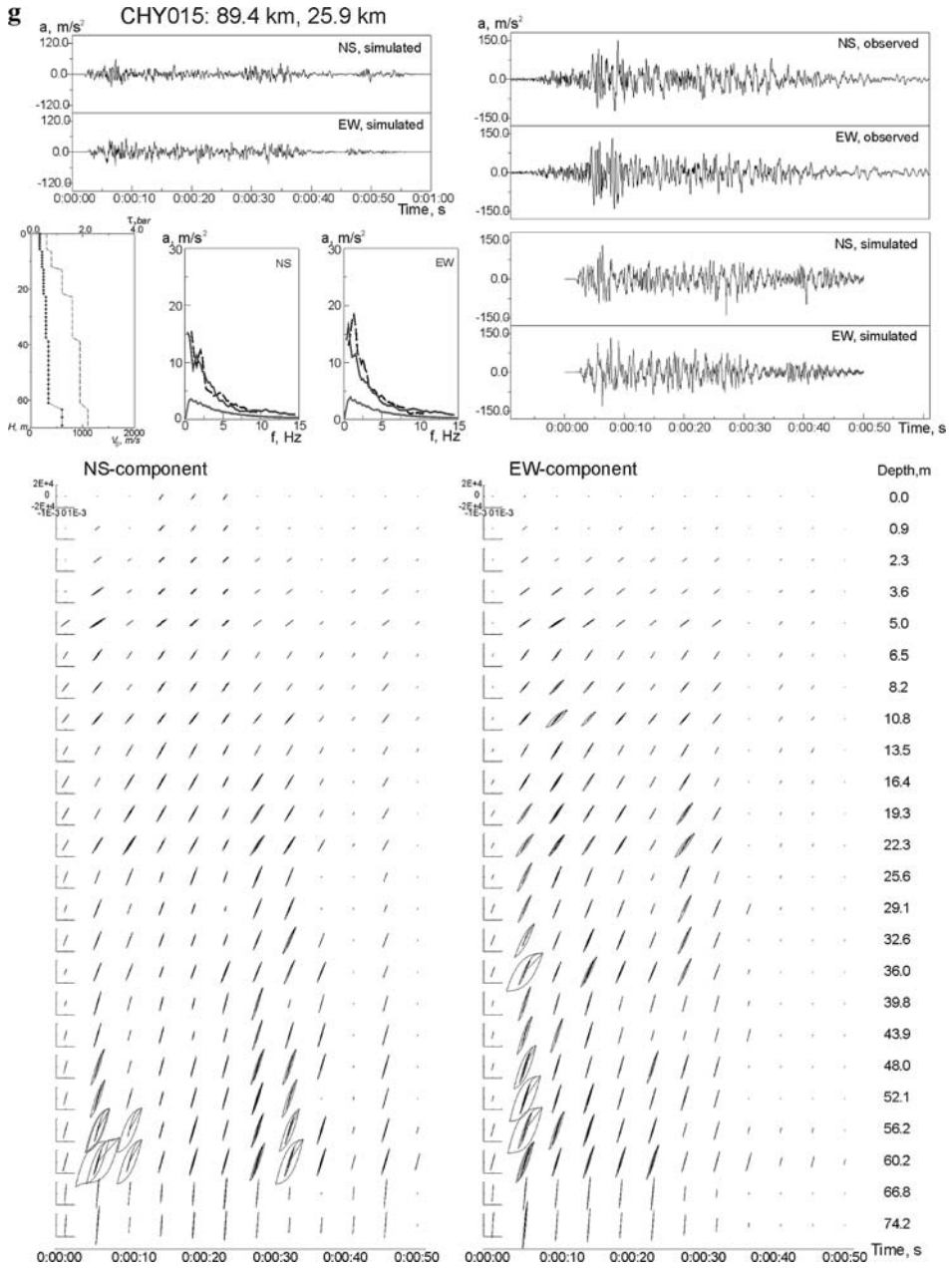

Figure 4
(Contd.)

underlying medium. This approximation, that allows no energy to be radiated back into the underlying medium, is rather accurate in this case, because the energy dissipation within the soil columns ($\sim$80–140 m) is rather high. Multiple reflections and resonances

occur in the upper tens of meters (down to $\sim$40–60 m), as will be shown below, and result in substantial losses of energy in these layers. Our preliminary calculations have also shown that the deviations from the case of the imposed motion (when motion at the base of the soil columns represents the sum of incident and reflected waves, and stress-strain relations in the soil layers are selected to fit observations on the surface and at the bottom of soil) are rather small.

Parameters, which were not known from measurements, but used in calculations, such as, τ_{max} and damping in the soil layers, were estimated based on available information on the characteristics of soil layers. To achieve a better agreement between the observations and simulations, sometimes we calculated the soil response to a number of simulated acceleration time histories within one series, in order to find the "best-fit" simulated accelerogram.

Analyzing vertical array records, we verified the validity of the assumed stress-strain relations in the soil layers by calculating deviations of the simulated accelerograms from the observed ones at depths of locations of the array devices. In the case of the Chi-Chi earthquake, only surface records are available, and they can be compared with the calculated soil response to simulated accelerograms, essentially stochastic signals. Therefore, to find the best fit to the observations, we compared the spectra, average intensities (as mean squares of acceleration time histories), and peak ground accelerations of the observed and simulated accelerograms at two horizontal components. These criteria were used to calculate a combined mean-square-root value of the deviation of the simulated spectra, average intensities, and peak ground accelerations from the observed ones at two horizontal components. This value was used as an estimate of the agreement between the observed and simulated acceleration time histories, and thus "the best-fit" stress-strain relations in the soil layers were selected, which are shown below as models of soil behavior. The observed and simulated accelerograms were analyzed on the whole, without dividing them into time intervals, as was done in the case of vertical array record analysis, because of the evident insufficiency of input information.

The results of simulation of acceleration time histories at soil sites are presented in Figure 4a-g. For each station, simulated accelerograms at the bottom of soil layers, observed and simulated accelerograms on the surface, and corresponding vertical distributions of stresses and strains in the soil layers, changing in time during the strong motion are shown for two horizontal components. The profiling data (*S*-wave velocities and shear stress in failure τ_{max} in the soil layers) and spectra of the observed and simulated (averaged over the series of simulated accelerograms) accelerograms are also shown. As explained above, to describe the behavior of each soil layer, only one stress-strain relation was used for all time intervals during the strong motion; however, in order to trace changes in soil behavior, working intervals of these stress-strain relations within twelve 4-second time intervals are presented for each soil layer (Fig. 4a-g).

At stations CHY026 and CHY104, surface accelerograms show the presence of intense seismic waves with periods of 3–5 seconds in oscillations at the surface (Fig. 4d, e). The stations are located to the southwest of the fault plane, in a valley, and these long-period

oscillations apparently represent standing waves due to *S*-wave reverberation in the basin sediments, i.e., basin-induced surface waves. These waves cannot be modeled in our 1-*D* simulations, and therefore, only the beginning part of the strong motion (15–20 sec.) is properly simulated at these stations. Spectra of the recorded accelerograms in Figs. 4d, e correspond to these beginning parts. As seen from the figures, in spite of the substantial uncertainty of the input information (motion at the bottom of the soil layers is estimated; shear stress in failure, damping in the soil layers, and models of the soil behavior are suggested), a fairly good agreement between the observed and simulated accelerograms is achieved at the studied stations.

We found that in the case of the Chi-Chi earthquake, even simple models, in which the behavior of all soil layers is described by the same stress-strain relation, are applicable to all the studied sites (i.e., show an agreement between observations and simulations), except TCU065, where the model is more complicated. At the TCU065 station, agreement between observations and simulations can only be obtained when describing the behavior of the upper ($\sim$37 m) and lower soil layers by different stress-strain relations.

Since the level of the underground water was close to the surface at all the stations ($V_P > 1300$ m/s in surface layers), "hard-type" stress-strain relations were applied to describe the soil behavior at all the stations. However, the stress-strain curves show substantial "hardening" (declinations to the stress axis) mostly at stations closest to the fault plane (TCU065 and TCU072), where the levels of the input motion were rather high. At these stations vertical distributions of stresses and strains in soil layers and spectra of oscillations at the bottoms and on the surfaces of soil profiles indicate resonant phenomena in the upper soil layers induced by the strong motion, which lead to amplification of seismic waves at $\sim$1–2 Hz at TCU065 and at $\sim$1–3 Hz at TCU072 (Fig. 4a, b). The "hard type" of soil behavior at these stations and rather low *S*-wave velocities ($\sim$200–250 m/s in the upper $\sim$10 m) stipulate a substantial amplification of oscillations on the surface. At TCU065 station, characteristic spiky waveforms in the acceleration time history are observed, which are often related to the strong nonlinearity of soil response (Archuleta, 1998) and to cyclic mobility and liquefaction of sandy surface soils (Lee *et al.*, 2001a).

As known, three main mechanisms of seismic wave transformation in subsurface soils are: (1) transition of seismic waves to upper soil layers with smaller values of $\bar{V}_S$ and density, ρ, leading to their amplification according to energy conservation law, (2) resonant phenomena in the upper soil layers also leading to amplification of seismic waves, (3) nonlinearity of soil response, often leading to de-amplification of seismic waves.

At TCU065 and TCU072 sites (and at many other sites, as shown below), we observe resonant phenomena in upper soil layers in conditions of strong nonlinearity of soil response.

Increase of the intensity of seismic oscillations due to resonant effects naturally leads to increasing nonlinearity of soil response; at the same time, nonlinearity decreases resonant frequencies of soil layers (if compared to "linear" soil response in weak

motion), which was noticed by many researchers. Thus, in cases of rather strong nonlinearity of soil response, resonant frequencies are related not only with geometrical and mechanical characteristics of the structure, but also with the intensity of "input" motion. In conditions of rather strong nonlinearity of soil response, spectra of oscillations on the surface tend to take the smoothed form $E(f) \sim f^{-n}$ (PAVLENKO and IRIKURA, 2005).

These transformations of spectra of seismic waves propagating in soil layers should be studied in special numerical experiments; in this paper, we can only establish facts of excitation of resonant oscillations in soil layers by the Chi-Chi earthquake. In this case, resonant oscillations (or resonant phenomena) mean trapping of seismic waves due to the impedance contrast between soft sediments and underlying denser layers. The interferences between these trapped waves lead to resonance patterns. These phenomena are clearly illustrated by spectra and vertical distributions of stresses and strains in soil layers shown in Figures 4 and 5. Comparison of spectra of oscillations at the bottoms and on the surfaces of soil layers reveals substantial amplification of their low-frequency components (up to 2–3 Hz, as seen from the figures); whereas vertical distributions of stresses and strains in soil layers indicate that maximum strains occur in the upper (resonating) layers, i.e., trapping of seismic waves in the upper layers.

At TCU138, amplification of seismic oscillations in the soil layers was not observed (Fig. 4c), because the soil profile represents mostly dense soils, even in the surface layers ($V_S \sim 400$ m/s). At stations: CHY026, CHY104, CHY074, and CHY015 amplification of seismic oscillations occurs at low frequencies, as seen from the spectra of oscillations on the surface and at the bottoms of the soil layers (Fig. 4d-g).

As seen from the figures, resonant oscillations were induced in the upper tens of meters (40–60 m) of soil at stations: TCU065, TCU072, CHY026, and CHY104 (actually, at all the stations except TCU138) during the earthquake. Maximum strains occurred at depths of ~5–10 m at TCU065 (~0.6%), ~8–12 m at TCU072 (0.3–0.4%), ~40–100 m at TCU138 (~0.1%), ~20 m at CHY026 (0.3–0.4%), ~10–15 m at CHY104 (0.2–0.3%), ~40 m at CHY074 (0.1–0.2%), and ~30–70 m at CHY015 station (0.1–0.2%).

According to our estimates, at TCU065, resonant phenomena occurred in the upper ~9 m of sandy clays with silt ($V_S \sim 200$ m/s) with maximum strains of ~0.6% (LEE *et al.*, 2001a, report liquefaction in the upper layers at this station). At the same time, resonant oscillations were also induced in the upper ~37 m (with V_s increasing from ~200 m/s to ~380 m/s) with maximum strains of ~0.2–0.4% (Fig. 4a).

At TCU072, resonances occurred in the upper ~11 m of the soft colluvium ($V_s \sim 250$ m/s), below which more dense breccia and shale layers are deposited ($V_s \sim 550$–700 m/s) (Fig. 4b). At CHY026 and CHY104, resonant oscillations were induced in the upper ~20 m (at CHY026, $V_s \sim 160$–240 m/s) and ~12 m (at CHY104, $V_s \sim 180$–190 m/s) of sandy clays with silt (Figs. 4d and e). At stations TCU138, CHY074, and CHY015, resonant phenomena were less pronounced and deeper: Maximum strains occurred at ~40–100 m at TCU138 (~0.1%), at ~40 m at CHY074 (~0.2%), and at ~30–70 m at CHY015 (0.1–0.2%). The corresponding stresses were as high as ~0.6–

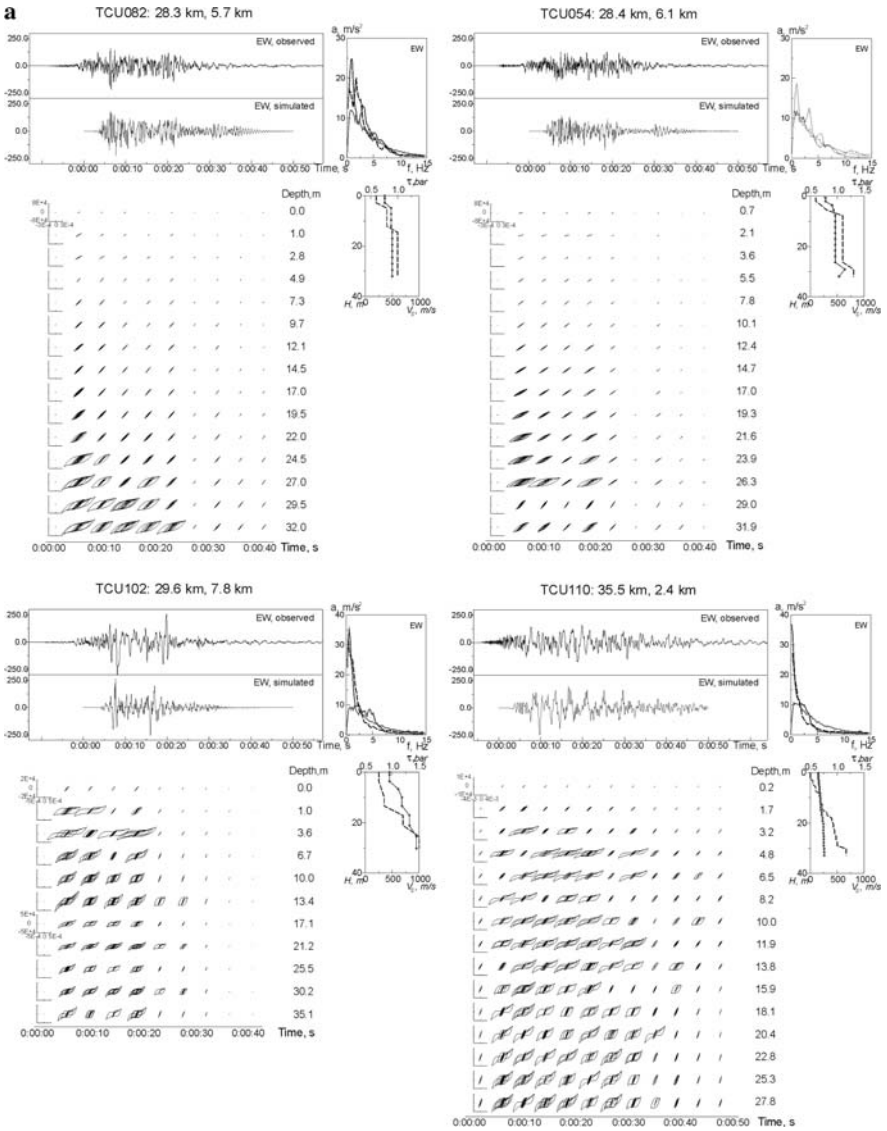

Figure 5

The results of simulations of acceleration time histories of the Chi-Chi earthquake at soil sites (EW component): The observed and simulated accelerograms on the surface (upper left corners), the corresponding vertical distributions of stresses and strains in the soil layers changing in time during the strong motion (below), spectra of the simulated accelerograms at the bottoms of the soil layers (low-level grey line) and of the observed (dashed line) and simulated (solid line) surface accelerograms (upper right corner), and the profiling data (below): V_s – solid line and τ_{max} – dashed line. a – TCU082, TCU054, TCU102, and TCU110, b – TCU116, TCU115, CHY025, and CHY092, c – CHY101, CHY002, CHY094, and CHY036, d - TCU033, CHY082, CHY027, and CHY032, e – CHY039, TCU017, CHY093, and CHY004, f – CHY033, CHY044, CHY055, and CHY012. After the station codes weighted average distances to the subfaults and distances to the closest subfaults are shown.

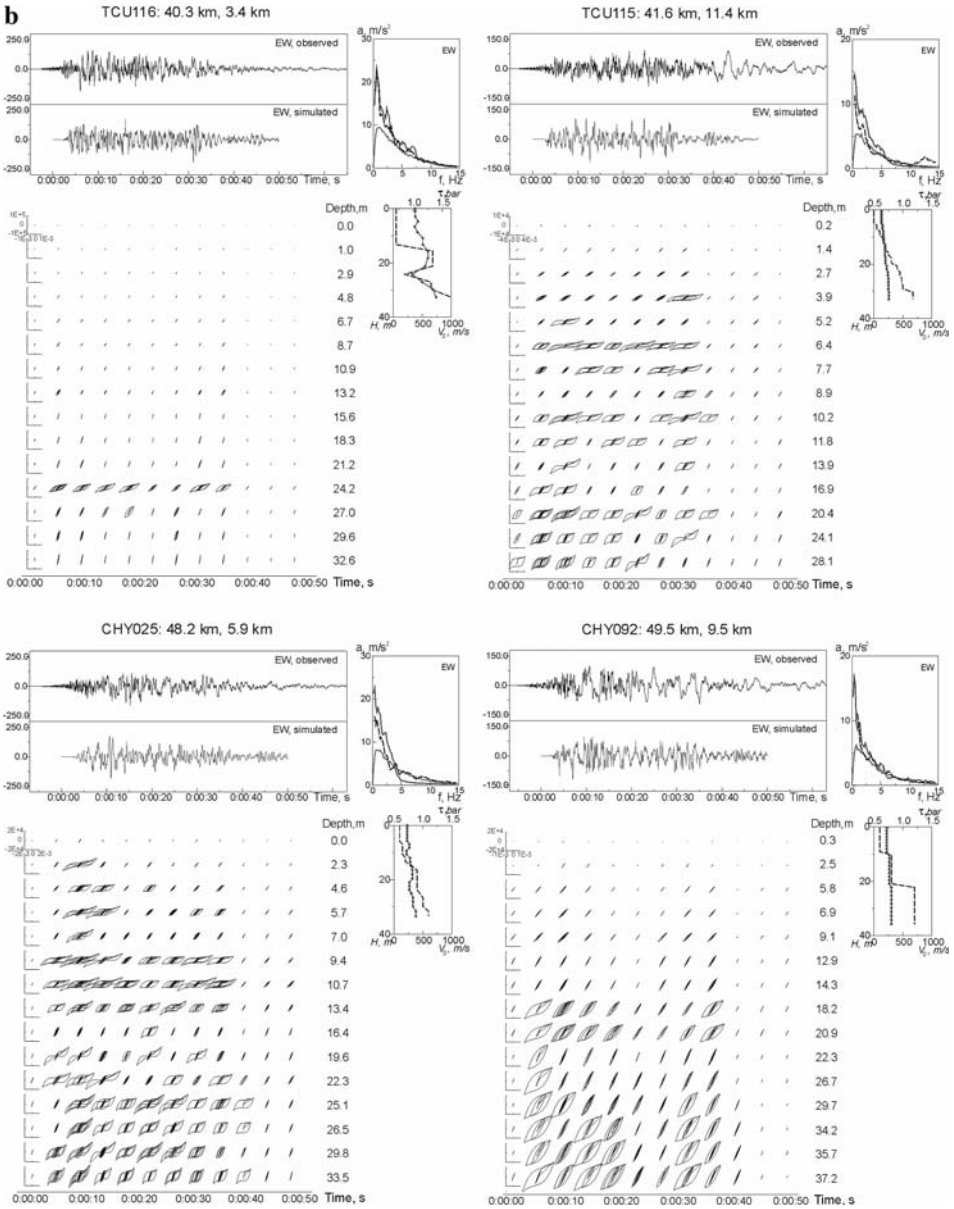

Figure 5
(Contd.)

1.2 bars, ∼0.4 bars, and 0.2–0.4 bars, respectively. At TCU138 and CHY074, resonating layers correlate with depths of slightly decreased *S*-wave velocities (Fig. 4c,f), whereas at CHY015 the whole upper part of the soil profile down to ∼60 m (V_s ∼170–340 m/s), underlayed by more dense soils (V_s > 600 m/s), is engaged into the resonant excitations

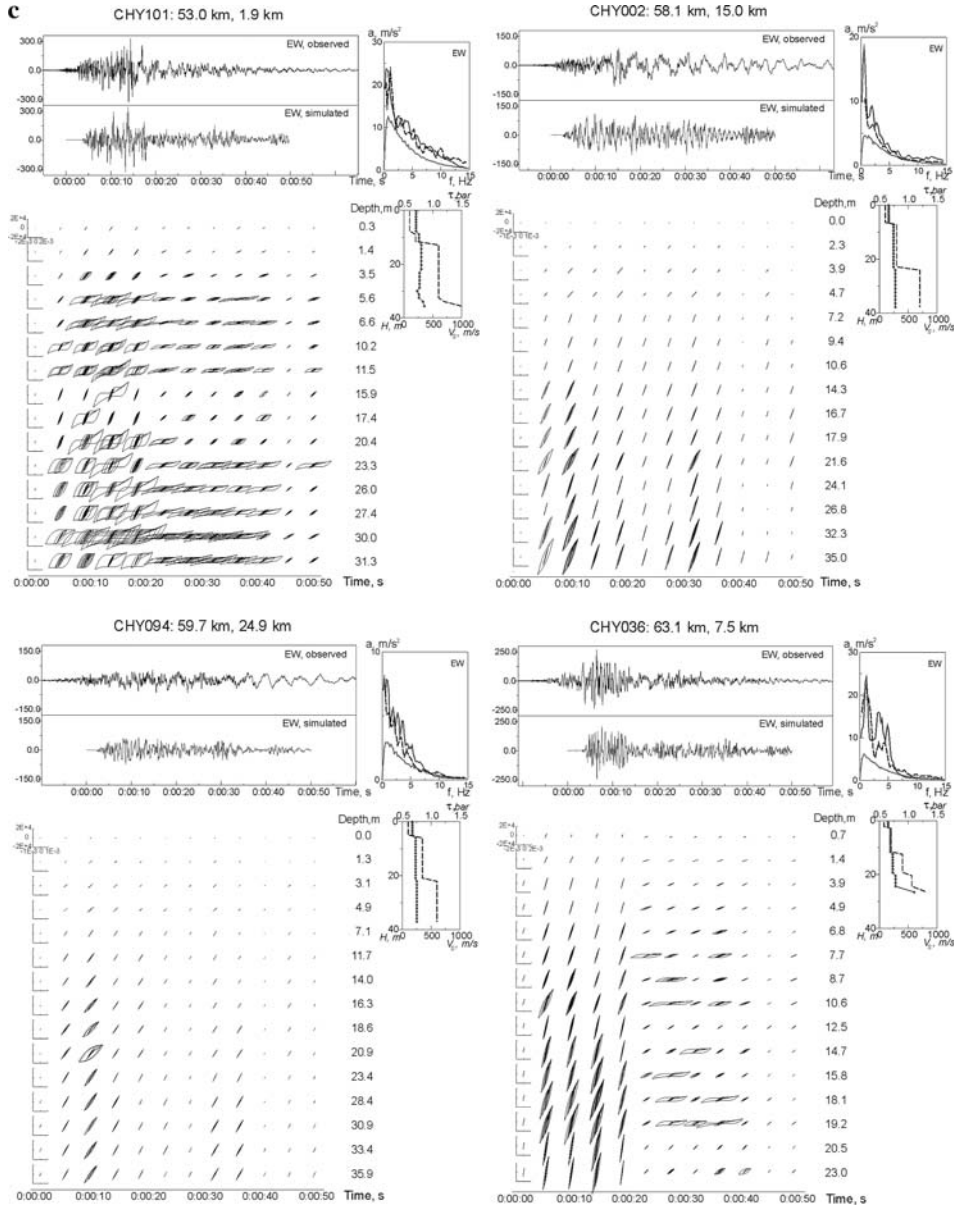

Figure 5
(Contd.)

(Fig. 4g). According to our estimates, resonant oscillations were induced by the Chi-Chi earthquake in the upper soil layers down to depths of $\sim$40–60 m at stations located within $\sim$30 km from the fault plane.

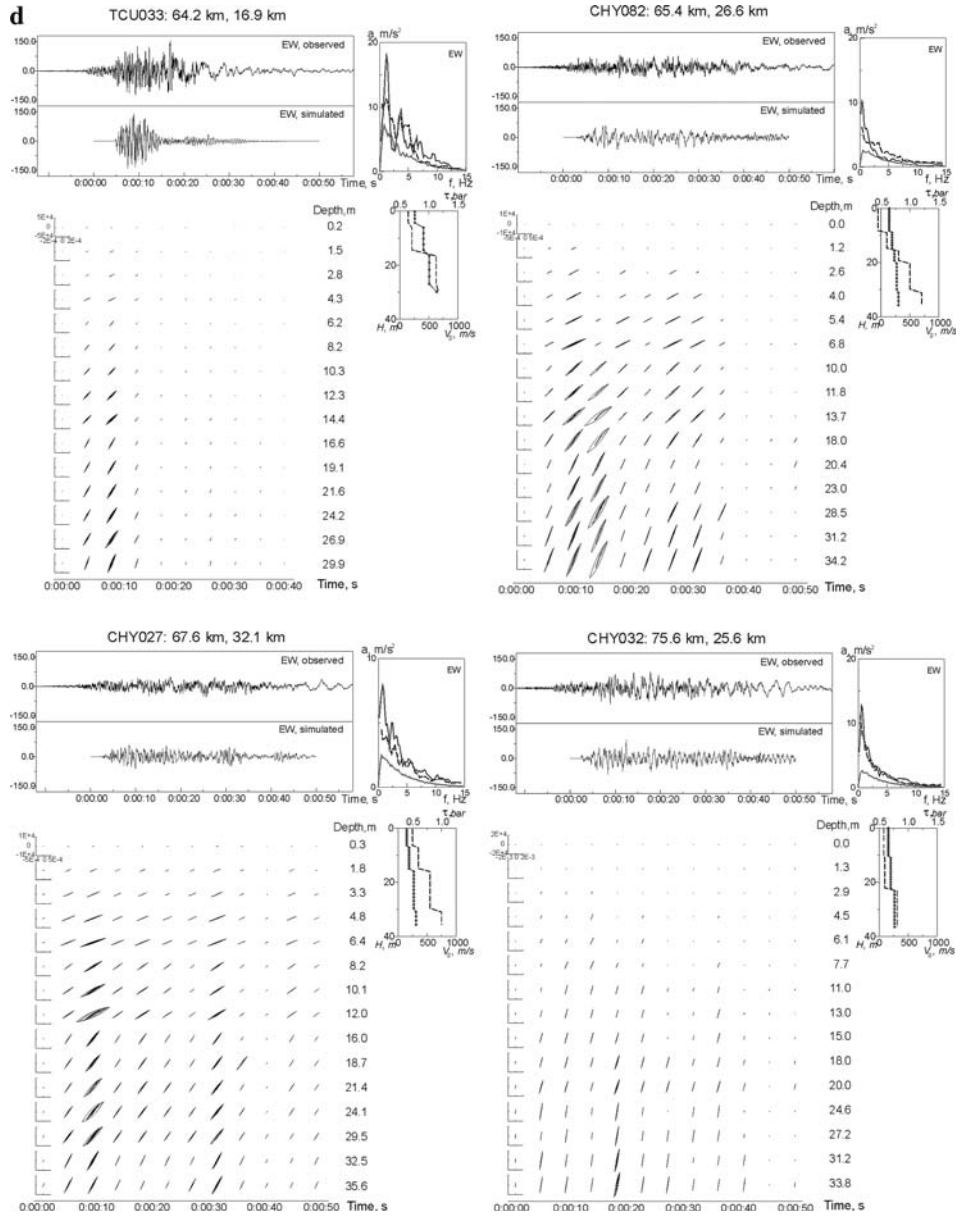

Figure 5
(Contd.)

As seen from Figures 4a-g, the strongest manifestations of soil nonlinearity were observed at stations TCU065, TCU072, and CHY074. Thus, strong nonlinearity of the soil behavior during the Chi-Chi earthquake was observed at Sites Class D (TCU065 and

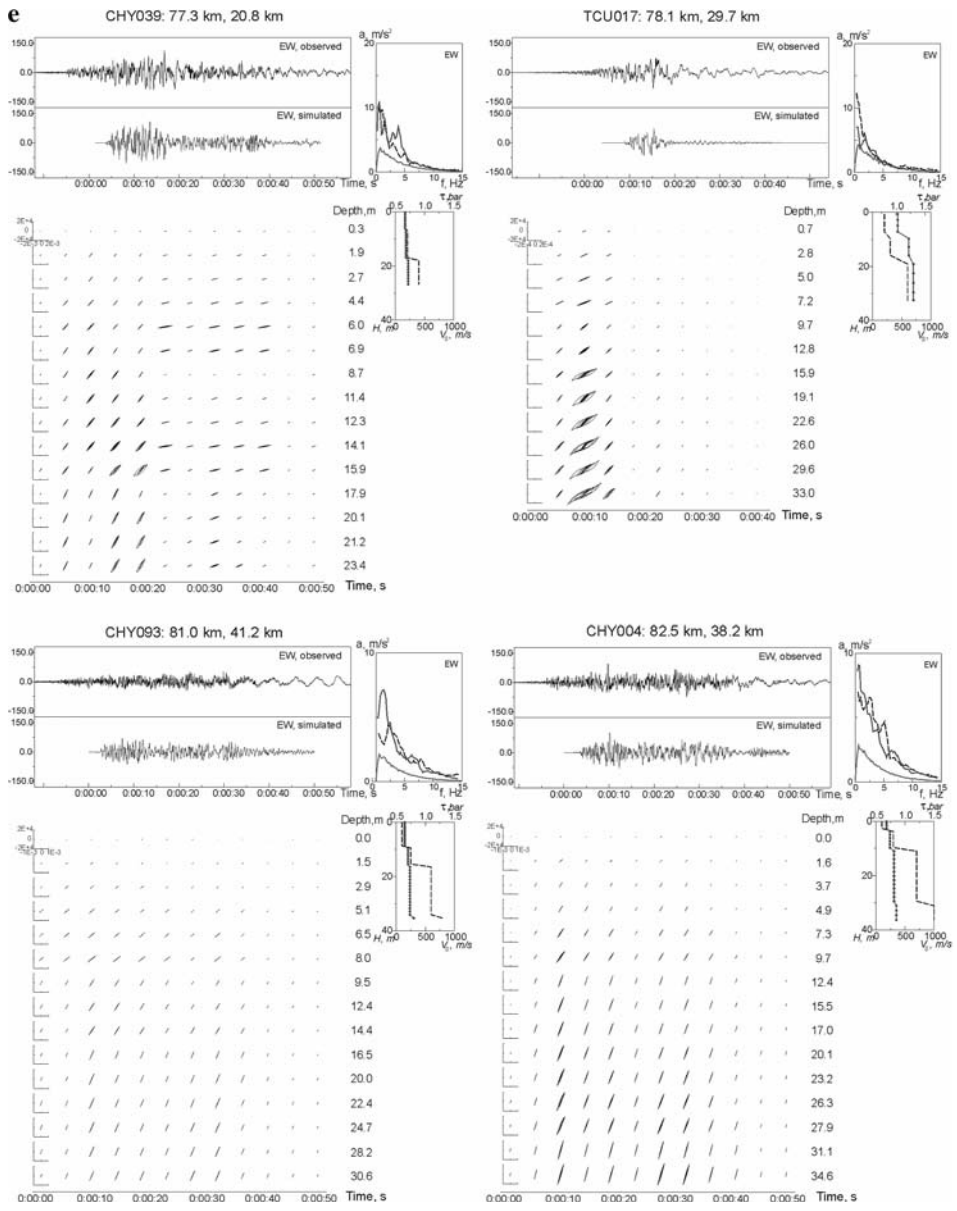

Figure 5
(Contd.)

TCU072) and Site Class C (CHY074); TCU065 did show liquefaction, and its possible classification as site class F is discussed in Lee *et al.* (2001a).

Since we have obtained realistic models of soil behavior at the seven stations possessing most complete information on the profiling data, we continued this study with

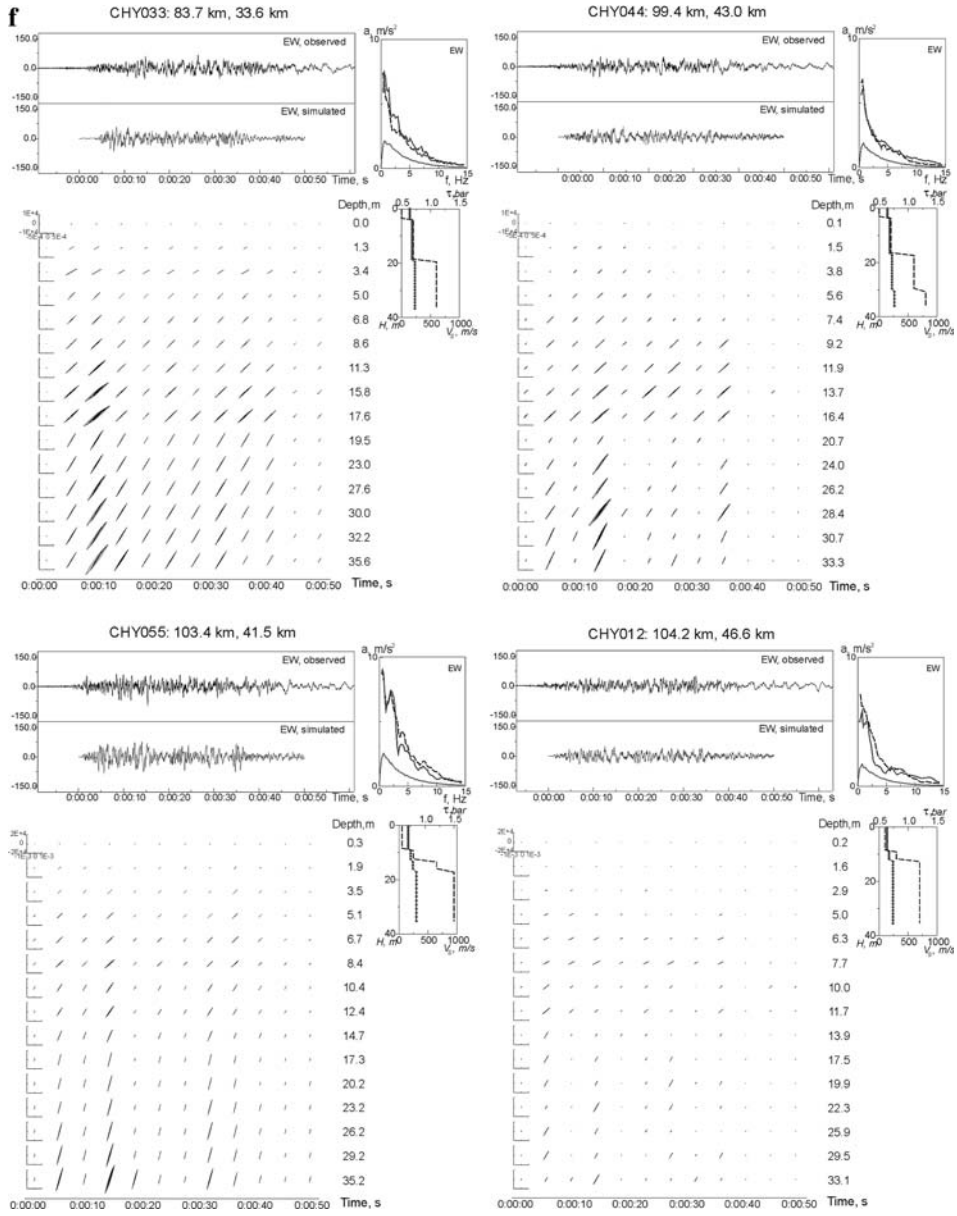

Figure 5
(Contd.)

additional twenty-four soil stations, for which the profiling data, *P*- and *S*-wave velocities and *SPT-N* testing results, were restricted to depths of $\sim$30–40 m. It was shown above that resonant oscillations were induced by the Chi-Chi earthquake in the upper soil layers

($\sim$40–60 m) in near-fault zones. Therefore, knowledge of soil parameters in the upper $\sim$30–40 m is not enough for calculations, and profiling data should be completed down to depths of at least $\sim$70–80 m. We reconstructed profiling data at depths $\sim$30–80 m based on the results by Lin *et al*. (2006), who conducted microtremor measurements at seven stations spaced at a distance of $\sim$120 km along the western coastal plain of Taiwan. Shallow *S*-wave velocity structures under all the studied sites down to $\sim$3 km were estimated by the inversion of dispersion curves obtained by frequency-wavenumber (*f-k*) analysis (Lin *et al*., 2006). The most reliable estimates of *S*-wave velocities were obtained for the upper $\sim$100 m, and they were verified by *P-S* logging data in the upper 40–70 m at some nearby TSMIP (Taiwan Strong Motion Instrumentation Program) stations. It was also found that the obtained *S*-wave velocity models correctly reflect the depths of major interfaces including the tops of Pliocene and Miocene (Lin *et al*., 2006). For the upper $\sim$100 m, fairly simple velocity structures and gradual increases of *S*-wave velocities with depth were found (Lin *et al*., 2006). This helped facilitate estimation of soil parameters at depths of $\sim$30–80 m. The validity of our assumptions is supported by the obtained (and discussed below) rather good agreement between simulated and observed accelerograms on the surface.

The results of simulation of acceleration time histories of the Chi-Chi earthquake at the twenty-four soil stations are presented in Figure 5a-f (only *EW* components are shown). For each station, the observed and calculated (one of the series of simulated accelerograms) acceleration records on the surface, their spectra and spectra of "input" motion at the bottoms of the soil layers (averaged over the series of simulated accelerograms), the profiling data (*S*-wave velocities V_s and shear stress in failure τ_{max} in the soil layers), as well as vertical distributions of stresses and strains in soil layers, changing in time during strong motion, are shown. Also, weighted average distances to all the subfaults of the fault plane and distances to the closest subfaults (considered as distances to the fault plane) are indicated.

As seen from the figures, in spite of the shortage of initial information, in some cases, a fairly good agreement was achieved between observations and simulations: For example, at stations: TCU082, TCU054, TCU102, TCU110 (Fig. 5a), TCU116, CHY025, TCU115, CHY092 (Fig. 5b), CHY101, CHY036 (Fig. 5c), CHY027, CHY032 (Fig. 5d), CHY039 (Fig. 5e), CHY033, CHY044, CHY055, and CHY012 (Fig. 5f). For other stations, the agreement between the observations and simulations is satisfactory.

At stations TCU115, CHY092, CHY002, CHY094, and CHY093 (Fig. 5b, c, e) final parts of records contain low-frequency intense seismic waves with periods of 3–5 seconds, which cannot be modelled in our 1-*D* simulations. These oscillations seem to represent effects of subsurface topography; they resemble basin-induced surface waves, i.e., standing waves due to *S*-wave reverberation in the basin sediments. This conclusion was made for stations CHY026 and CHY104 (Fig. 4d,e). Such waves can also be distinguished, though not so clearly, at stations CHY082, CHY027, and CHY032 (Fig. 5d). All these stations are located in a valley (elevations 4–34 m), close to each

other, and this area is marked by grey color in Figure 1. At these stations, the soil composition in the upper ~30–40 m is similar: Predominantly silty soils with sands and clays and with average *S*-wave velocities of ~190–260 m/s (Table 3). For these stations, spectra were calculated based on the beginning parts of records, not containing basin waves.

Long-period seismic waves are also noticed in the final parts of records at stations of the "northern" group, TCU033 and TCU017 (Fig. 5d and e). LEE *et al*. (2001) attribute station TCU017 to a typical case of a tree root problem, where the concrete slab base of the station is affected by tree roots; it is not clear if basin waves are affecting records at these stations. An agreement between observations and simulations was obtained for the beginning parts of records at both of these stations; and spectra were estimated based on these beginning parts. At the same time, the duration of the simulated strong ground motion at both stations is shorter than that of the observed ones. This is a problem at all rock and soil stations of the "northern" group. Apparently, this is due to some inconsistency in the applied model of slip distribution over the fault plane.

At stations CHY101, CHY036, and CHY039 (Fig. 5c,e), the recorded accelerograms possess characteristic shapes, such as, intense beginning parts (first 15–20 sec. of the strong motion) and final parts of substantially smaller intensity, whereas the intensities of "input" motions at the three stations (simulated accelerograms not shown) remained at almost the same levels during the earthquake. We found that simulation of the recorded accelerograms at the three stations with one stress-strain relation applied at all time intervals during the strong motion is not possible; therefore, the beginning and final parts of these records were simulated separately. It was found that for the final parts of records, an agreement between observations and simulations can only be achieved, if describing the soil behavior by very slight stress-strain relations, with slopes close to horizontal ones (Fig. 5c and e). A similar case was the simulation of soil behavior at the Port Island vertical array site during the Kobe earthquake. At Port Island, liquefaction in the upper soil layers (~13 m) occurred, and the behavior of these layers was described by similar very slight stress-strain relations (PAVLENKO and IRIKURA, 2003).

All three stations, CHY101, CHY036, and CHY039, are located close to each other, in a bajada stretched at the southwestern corner of the fault, and their elevations are 75 m, 45 m, and 16 m, respectively (Fig. 1). The upper parts of the soil profiles represent silty soils with sands and clays with average *S*-wave velocities of ~200–280 m/s (Table 3), underlayed by gravels and dense clays at depths of ~26–34 m. Resonant oscillations were induced in the upper softer layers during the strong motion, and maximum strains achieved ~0.8% at CHY101 station (with stresses up to ~0.4 bars), ~0.6% at CHY036 station (with stresses up to ~0.4 bars), and ~0.3% at CHY039 station (with stresses of ~0.1 bars), according to our estimates. Evidently, the obtained results may indicate liquefaction phenomena occurring at stations CHY101, CHY036 and CHY039 during the Chi-Chi earthquake (Fig. 5c and e), though there is likely another possible explanation.

The highest strains were achieved in the upper ~30–40 m at stations TCU065 (~0.6%), TCU110 (~0.6–0.8%), and TCU115 (~0.6–0.8%) (Fig. 5a, b), possessing

similar models of soil behavior, such as, expressed resonant oscillations induced by strong motion: in the upper ~9 m and ~37 m at TCU065 station, in the upper ~30–40 m at stations TCU110 and TCU115. The soil composition of the upper layers is similar at these stations: mostly sandy, clayey, and silty soils with average *S*-wave velocities of ~300 m/s at TCU065 and 190–210 m/s at TCU110 and TCU115 stations (Table 3).

Lee *et al*. (2001) reported liquefaction occurred at stations TCU065 and TCU110 (Figs. 4a and 5a) during the Chi-Chi earthquake. The constructed models of soil behavior at these stations confirm this conclusion. At TCU115 station (Fig. 5b) strains in the surface layers (in the upper meters) are not as high as at TCU065 and TCU110 stations, because it is located at a larger distance from the fault plane than TCU065 and TCU110 (Table 3). Liquefaction effects are not as clearly expressed at TCU115 as at TCU065 and TCU110, and they involve deeper layers. The constructed models of soil behavior at these stations indicate that resonant oscillations induced by strong motion in the upper soft layers are accompanied by large strains and pore pressure build-up, leading to cyclic mobility and liquefaction of the water-saturated sandy soils (Fig. 5a and b). Similar phenomena are also observed at TCU102 (strains in the upper layers of ~0.2%) (Fig. 5a), CHY025 (strains ~0.4%) (Fig. 5b), and at stations TCU072 (strains ~0.3–0.4%) and CHY026 (strains ~0.3–0.4%), as discussed above. At other stations, maximum strains in the upper soil layers did not exceed ~0.2%, according to our estimates.

Thus, we can conclude that resonant oscillations were induced by the Chi-Chi earthquake in the soil layers down to ~40–60 m in the near-fault zones. As seen from Figures 4 and 5, resonant phenomena occurred in the upper soft soil layers (with average *S*-wave velocities not exceeding ~300 m/s), and the resonances were most pronounced at stations located within ~20–22 km from the fault plane, such as, at: TCU065, TCU110, TCU115, CHY025, CHY092, CHY101, CHY026, CHY036, and CHY039. Since at these soil sites resonant phenomena occurred in conditions of a rather strong nonlinearity of soil behavior (as seen from Figures 4 and 5), substantial changes in spectral composition of seismic waves propagating in soil layers appeared: Spectra of oscillations on the surface took forms close to $E(f) \sim f^{-n}$, i.e., resonant amplification was observed in the low-frequency range, up to 2–3 Hz (Figs. 4 and 5).

At some of these stations closest to the fault plane (TCU065, TCU110, TCU115, CHY025, CHY101, and CHY036), our simulations indicate more complicated soil behavior, i.e., the behavior of different (in their properties) soil layers described by different stress-strain relations. Different stress-strain relations were applied to describe the behavior of soil layers in cases when the upper sandy-clayey-silty resonating layers were underlayed by more dense layers (with *SPT-N* > 50): silty clays (as at TCU065 station), and gravels (as at stations CHY025, CHY101, and CHY036), etc.

On the whole, we found that soil behavior in near-fault zones during the Chi-Chi earthquake was rather simple, i.e., at the majority of the studied soil stations, the behavior of all the layers (upper tens of meters) could be satisfactorily described by a single

stress-strain relation. However, if we possessed more complete information (for example, vertical array records down to ~80–100 m were available), we could reconstruct the soil behavior in more detail. Apparently, we would obtain changes in stress-strain relations describing the soil behavior during the strong motion, as was obtained in analysis of the Kobe and Tottori earthquakes (PAVLENKO and IRIKURA, 2003, 2004). Evidently, the approximation of "one stress-strain relation" could be improved upon. Therefore, in this study we estimate some averaged-in-time and smoothed characteristics of soil behavior. These characteristics are also somewhat approximate, because of the insufficiency of the initial information: Acceleration time histories at the bottoms of soil layers and the profiling data down to ~70–80 m at some stations are approximated in our study.

Thus, valuable data on *in situ* soil behavior during the Chi-Chi earthquake is obtained, and it can be compared with models of soil behavior during the 1995 Kobe ($M_w = 6.8$) and 2000 Tottori ($M_w = 6.7$) (Japan) earthquakes obtained in previous studies (PAVLENKO and IRIKURA, 2003, 2004, 2005, 2006).

At most of the studied stations in the near-fault zones of the Kobe and Tottori earthquakes, surface soil layers represented sandy water-saturated soils (the levels of underground water were less than ~10 m), and during strong ground motion, pore pressure build-up occurred in the upper soft layers, and the soil behavior was of the "hard-type", most expressed in near-fault zones. In the upper soil layers, resonant oscillations were induced by the strong motion, and amplitudes of oscillations in the upper ~10–15 m and on the surface were high. This kind of soil behavior was clearly observed at the SGK vertical array (~6 km from the fault plane) during the Kobe earthquake (PAVLENKO and IRIKURA, 2003) and at the Kik-Net stations TTRH02 and SMNH01 (~7 km and ~8 km from the fault plane, respectively) during the Tottori earthquake (PAVLENKO and IRIKURA, 2004, 2006).

During the Chi-Chi earthquake, resonant phenomena involved not only the upper ~10–15 m, as in the near-fault zones of the Kobe and Tottori earthquakes, but much thicker layers, up to ~40–60 m. Resonance effects of increasing amplitudes of oscillations on the surface combined with "hard-type" soil behavior, are most pronounced at stations closest to the fault plane (distances < 10 km from the fault plane) and are still observed at distances of ~10–16 km from the fault. At other (remote) stations, such effects also occur but are less pronounced because they decrease with increasing the distance from the fault plane. The "hard" character of soil behavior virtually disappears at distances greater than ~12 km from the fault plane, and at distances of more than ~30–40 km, oscillations in the soil layers become very close to linear ones. A similarity in the behavior of similar soils during these three earthquakes is observed, indicating a possibility of forecasting soil behavior in future strong earthquakes.

The constructed models of soil behavior allow estimation of various important parameters, characterizing soil response during the Chi-Chi earthquake, such as, amplification of seismic waves in soil layers, average and maximum stresses and strains induced by the strong motion in soil layers at different depths down to ~70–80 m, shear

moduli reduction, nonlinear components of soil response, and others. The distribution of these parameters around the fault plane and their dependencies on the distance from the fault can be obtained and analysed. All these problems will be discussed in our next paper, which is now in preparation.

4. Conclusions

Thus, acceleration time histories at rock and soil stations in near-fault zones of the Chi-Chi earthquake are simulated, and models of the soil behavior are constructed, i.e., vertical distributions of stresses and strains in the soil layers down to $\sim$70–140 m are estimated at thirty one soil sites located within $\sim$50 km from the fault.

Because of the essentially stochastic character of the simulated acceleration time histories, the constructed models of the nonlinear soil behavior can be treated as an approximation to reality. However, a fairly good agreement was obtained between spectra of the observed and simulated accelerograms and even between their waveforms, which testifies to the validity of the obtained representations and allows us to make some definitive conclusions.

A decreased attenuation of seismic waves due to geometrical spreading, less than that described by the relationships $1/r$ for $r < 50$ km, $1/50$ for $50 \leq r < 150$ km, was found at stations in the near-fault zones of the Chi-Chi earthquake, which was apparently due to the effects of the fault zone geometry.

A decreased (compared to other Sites Class B) crustal amplification was established at stations: TCU049, TCU053, TCU046, HWA023, HWA024, and CHY110, indicating probable "hard rock" Sites Class A.

In spite of the large magnitude of the Chi-Chi earthquake and the proximity of the studied soil stations to the fault plane (and therefore, strong "input" motion), the soil behavior at the studied sites was found to be relatively simple, i.e., an agreement between the observed and simulated accelerograms was obtained even in cases of using only one stress-strain relation for describing the behavior of all the soil layers down to $\sim$70–80 m at all time intervals during strong motion. Obviously, this is due to the homogeneity of the characteristics of the soil layers in depth.

At all the studied stations, soil behavior during the Chi-Chi earthquake was defined by resonant oscillations of soil layers and nonlinearity of soil response. Resonant oscillations were induced in the upper meters of soil profiles (down to $\sim$40–60 m); strains achieved $\sim$0.6% in the vicinity of the fault plane, at TCU065, and 0.1–0.4% at other stations located within $\sim$30 km of the fault. At near-fault stations the relationships between the stresses and the strains and the soil behavior were substantially nonlinear.

Liquefaction phenomena were identified at TCU065, TCU110, TCU115, CHY101, CHY036, and CHY039 stations, where estimated strains achieved $\sim$0.6–0.8%; at other stations, maximum strains in the soil layers did not exceed 0.1–0.4%, according to our estimates.

Thus, the constructed models of soil behavior in the near-fault zones of the Chi-Chi earthquake add to our representations of soil behavior during strong ground motion, and allow for comparisons with soil behavior in the near-fault zones of the Kobe and Tottori earthquakes, estimated based on vertical array data, with the obtained data of soil behavior during the Chi-Chi earthquake. In the near-fault zones of the three earthquakes, "hard-type" soil behavior is prevalent along with resonant oscillations in the upper surface layers; both of which represent unfavourable factors that lead to high acceleration amplitudes on the surface. Also, a similarity in the behavior of similar soils during the Kobe, Tottori, and Chi-Chi earthquakes was found, indicating the possibility of forecasting soil behavior in future earthquakes.

Acknowledgements

This research was supported by the National Science Council (Taiwan) under Grant No. NSC 95-2811-M-492-001. The profiling data at soil stations provided by NCREE are greatly appreciated.

References

Anderson, J. G. and Hough, S. E. (1984), *A model for the shape of the Fourier amplitude spectrum of acceleration at high frequencies*, Bull. Seismol. Soc. Am. *74*, 5, 1969–1993.

Archuleta, R. J. (1998), *Direct observations of nonlinearity in accelerograms*. In *The Effects of Surface Geology on Seismic Motion* (eds. Irikura, Kudo, Okada and Sasatani), (Balkema, Rotterdam 1998) pp. 787–792.

Boore, D. M. (2003), *Simulation of ground motion using the stochastic method*, Pure Appl. Geophys. *160*, 635–676.

Boore, D. M. and Joyner, W. B. (1997), *Site amplifications for generic rock sites*, Bull. Seismol. Soc. Am. *87*, 2, 327–341.

Bazzurro, P., Sjoberg, B., and Luco, N. (2001), *Post-elastic response of structures to synthetic ground motions*, http://geohazards.cr.usgs.gov/staffweb/nluco/manuscripts/0409–Bazzurro+Sjoberg+Luco.pdf.

Chen, K. C., Shin, T. C., and Wang, J. H. (1989), *Estimates of coda Q in Taiwan*, Proc. Geol. Soc. China. *32*, 339–353.

Chi, W.-C., Dreger, D., and Kaverina, A. (2001), *Finite-source modeling of the 1999 Taiwan (Chi-Chi) earthquake derived from a dense strong-motion network*, Bull. Seismol. Soc. Am. *91*, 5, 1144–1157.

Chiu, H. C. (2001), *Data Files from the SMART-2 Strong Motion Array for the Chi-Chi Earthquake*, Bull. Seismol. Soc. Am. *91*, 5, 1391–1392.

Gusev, A. A. and Pavlov, V. M. (2008), *Broad band Simulation of Earthquake Ground Motion by a Spectrum-Matching, Multiple-Pulse Technique*, Earthquake spectra.

Hardin, B. O. and Drnevich, V. P. (1972), *Shear modulus and damping in soils: Design equations and curves*, Proc. Am. Soc. Civil Eng., J. Soil Mech. Found. Div. *98*, 667–692.

Joyner, W. B. and Chen, T. F. (1975), *Calculation of nonlinear ground response in earthquakes*, Bull. Seismol. Soc. Am. *65*, 1315–1336.

Lee, W. H. K., Cheng, C.-T., Liao, C.-W., and Tsai, Y.-B. (2001a), *Site classification of Taiwan free-field strong-motion stations*, Bull. Seismol. Soc. Am. *91*, 5, 1283–1297.

Lee, W. H. K., Shin, T. C., Kuo, K. W., Chen, K. C., and Fu, C. F. (2001b), *CWB free-field strong-motion data from the 21 September Chi-chi, Taiwan, earthquake*, Bull. Seismol. Soc. Am. *91*, 5, 1370–1376.

LIN C.-M., WEN, K.-L., and CHANG, T.-M. (2006), *Estimation of S-wave velocity model in the western coastal plain of Taiwan*, Third Intern. Conf. on Urban Earthquake Engineer, Center for Urban Earthquake Engineering, Tokyo, 617–622.

MA, K.-F., MORI, J., LEE, S.-J., and YU, S. B. (2001), *Spatial and temporal distribution of slip for the 1999 Chi-Chi, Taiwan, earthquake*, Bull. Seismol. Soc. Am. *91*, 5, 1069–1087.

OGLESBY, D. and DAY, S. (2001), *Fault geometry and the dynamics of the 1999 Chi-Chi (Taiwan) earthquake*, Bull. Seismol. Soc. Am. *91*, 5, 1099–1111.

PAVLENKO, O. V. and IRIKURA, K. (2003), *Estimation of nonlinear time-dependent soil behavior in strong ground motion based on vertical array data*, Pure Appl. Geophys. *160*, 2365–2379.

PAVLENKO, O. V. and IRIKURA, K. (2004), Identification of the nonlinear behavior of soils in near-fault areas during the 2000 Tottori Earthquake, Proc. of the 11th Intern. Conf. on Soil Dynamics and Earthquake Engineering and the 3d Intern. Conf. on Earthquake Geotechnical Engineering, 7–9 Jan. 2004, Univ. of California, Berkeley, USA, pp. 201–207.

PAVLENKO, O. V. and IRIKURA, K. (2005), *Identification of the nonlinear behavior of liquefied and non-liquefied soils during the 1995 Kobe earthquake*, Geophys. J. Intern. *160*, 539–553.

PAVLENKO, O. V. and IRIKURA, K. (2006), *Nonlinear behavior of soils revealed from the records of the 2000 Tottori, Japan, Earthquake at stations of the digital strong-motion network Kik-Net*, Bull. Seismol. Soc. Am. *96*, 6, 2131–2145.

PAVLENKO, O. V. and LOH, C.-H. (2005), *Nonlinear identification of the soil response at Dahan downhole array site during the 1999 Chi-Chi earthquake*, Soil Dynamics and Earthquake Engin. *25*, 3, 241–250.

ROUMELIOTI, Z. and BERESNEV, I. A. (2003), *Stochastic finite-fault modeling of ground motions from the 1999 Chi-Chi, Taiwan, Earthquake: Application to rock and soil sites with implications for nonlinear site response*, Bull. Seismol. Soc. Am. *93*, 4, 1691–1702.

WANG, W.-H., CHANG, S-H., and CHEN, C.-H. (2001), *Fault slip inverted from surface displacements during the 1999 Chi-Chi, Taiwan, earthquake*, Bull. Seismol. Soc. Am. *91*, 5, 1167–1181.

WU, C., TAKEO, M., and IDE, S. (2001), *Source process of the Chi-Chi earthquake: A joint inversion of strong motion data and global positioning system data with a multifault model*, Bull. Seismol. Soc. Am. *91*, 5, 1128–1143.

ZENG, Y. and CHEN, C.-H. (2001), *Fault rupture of the 20 September 1999 Chi-Chi, Taiwan, earthquake*, Bull. Seismol. Soc. Am. *91*, 5, 1088–1098.

(Received April 7, 2007; accepted October 29, 2007)

To access this journal online:
www.birkhauser.ch/pageoph